

Less atmospheric radiative heating by dust due to the synergy of coarser size and aspherical shaped dust with coarser size

Akinori Ito¹, Adeyemi A. Adebisi^{2,3}, Yue Huang², and Jasper F. Kok²

¹Yokohama Institute for Earth Sciences, JAMSTEC, Yokohama, Kanagawa, 236-0001, Japan.

²Department of Atmospheric and Oceanic Sciences, University of California, Los Angeles, CA 90095, USA.

³Department of Life and Environmental Sciences, University of California - Merced

Correspondence to: Akinori Ito (akinorii@jamstec.go.jp)

Abstract. Mineral dust aerosols cool and warm the atmosphere by scattering and absorbing ~~both~~ solar (short-wave: SW) and thermal (long-wave: LW) radiation. However, ~~significant~~~~large~~ uncertainties remain in dust radiative effects, largely due to differences in the dust size distribution and spectral optical properties simulated in Earth system models. Dust models typically underestimate the coarse dust load (more than 2.5 μm in a diameter) and assume a spherical shape, which leads to an overestimate of the fine dust load (less than 2.5 μm) after the dust emissions in the models are scaled to match observed dust aerosol optical depth at 550 nm (DAOD₅₅₀). Here, we improve the simulated dust properties with datasets that leverage measurements of size-resolved dust concentration, ~~and~~ asphericity factor, ~~and refractive index (improved simulation)~~ in a coupled global chemical transport model (~~IMPACT~~) with a radiative transfer module (~~RRTMG~~) (~~default simulation~~). After the adjustment of size-resolved dust concentration and spectral optical properties, ~~The~~ the global and annual average of ~~dust aerosol optical depth at 550 nm (DAOD₅₅₀)~~ from the ~~improved~~ simulation increases from 0.023 to 0.029, ~~and~~ falls within the range of a semi-observationally-based estimate (0.030 ± 0.005), ~~in contrast to that (0.023) of the default simulation.~~ The reduction of fine dust load after the adjustment leads to a reduction of the SW cooling at the Top Of the Atmosphere (TOA). To improve agreement against a semi-observationally-based estimate of the radiative effect efficiency at TOA, we find that was obtained using a less absorptive SW and more absorptive LW dust refractive indices is required for coarser aspherical dust. Thus, only a minor difference is estimated for the net global dust radiative effect at the Top Of Atmosphere (TOA) on a global scale to the default simulation (-0.08 vs. -0.009 $\text{W}\cdot\text{m}^{-2}$ on a global scale) but. Conversely, our sensitivity simulations reveal that the surface warming is substantially enhanced near the strong dust source regions the net global dust radiative effect results in less cooling at the surface (less cooling to -0.23 vs. from -0.6088 $\text{W}\cdot\text{m}^{-2}$ on a global scale). Thus, less atmospheric radiative heating is estimated near the major source regions (less heating to 0.15 from 0.59 $\text{W}\cdot\text{m}^{-2}$ on a global scale), because of enhanced LW warming at the surface by the synergy of coarser size and aspherical dust shape. Our results thus suggest less atmospheric radiative heating due to aspherical dust with coarser size over the major source regions (0.15 vs. 0.79 $\text{W}\cdot\text{m}^{-2}$ on a global scale).

1 Introduction

Mineral dust aerosols can both cool and warm the climate, but how much dust aerosols net influence global climate is highly uncertain (Penner, 2019). Global dust modeling studies have suggested that mineral dust exerts ~~an~~ global and annual mean aerosol radiative effect (RE) between -0.6 and $+0.2 \text{ W m}^{-2}$ at the Top Of the Atmosphere (TOA) and between -0.2 and -2.7 W m^{-2} at the surface (Miller and Tegen, 1998; Balkanski et al., 2007; Tanaka et

37 al., 2007; Takemura et al., 2009; Räisänen et al., 2013; Zhao et al., 2013; Albani et al., 2014; Colarco et al., 2014;
38 Heald et al., 2014; ~~Tuccella et al., 2019~~; Di Biagio et al., 2020; Tuccella et al., 2020). Whereas a negative RE
39 corresponds to the cooling of the global system when the sunlight is reflected to space, a positive RE corresponds to
40 an overall warming of the Earth-atmosphere system by trapping incident short-wave (SW) and outgoing long-wave
41 (LW) radiation. Radiative effect by dust aerosols perturbs surface temperature, wind speed, rainfall, and vegetation
42 cover, which may induce feedback on dust emissions (Perlwitz et al. 2001; Miller et al., 2004a; Colarco et al., 2014).
43 The climate feedback does not only depend ~~only~~ on RE at TOA or the surface alone, but also on ~~its~~ the difference to
44 the ~~surface~~ value at TOA and surface, which represents radiative heating within the atmosphere (Miller et al., 2004b;
45 Yoshioka et al., 2007; Lau et al., 2009). The large uncertainties in quantifying the dust RE in the models are mainly
46 propagated from the large spatial heterogeneity and temporal variability of mineral dust abundance and the
47 physicochemical properties (e.g., size distribution, mineral composition, and shape), as well as the ground surface
48 characteristics and atmospheric properties (e.g., surface reflectance, temperature, and atmospheric absorption) (Sicard
49 et al., 2014; Lacagnina et al., 2015; Li and Sokolik, 2018). The model errors in dust size distribution and particle shape
50 can lead to an overestimate of fine dust load after the dust emissions in the models are scaled to match observed dust
51 aerosol optical depth at 550 nm (DAOD₅₅₀). The corresponding overestimate of SW cooling might be compensated
52 for in models by using a refractive index that is too absorbing (Di Biagio et al., 2019, 2020), which depends on the
53 mineral composition of the dust. We regard “fine” and “coarse” dust as dust particles with a diameter less than 2.5
54 µm (i.e., PM_{2.5}) and between 2.5 and 20 µm, respectively. Below, we provide a brief discussion of the effects of the
55 dust size distribution, particle shape~~mineral composition~~, and mineral composition ~~particle shape~~ on dust radiative
56 effects.

57 Recently~~First~~, there has been increased attention paid to the importance of accurately predicting the abundance
58 of coarse dust for the global energy balance (Kok et al., 2017; Song et al., 2018; Di Biagio et al., 2020; Adebisi and
59 Kok, 2020). The coarser particles are expected to be more prevalent closer to the source regions, as they fall ~~downward~~
60 much faster than finer particles (Mahowald et al., 2014). For instance, the lifetime of dust aerosols larger than 30 µm
61 in diameter is less than 12 h in most cases except in large haboobs (Ryder et al., 2013). Current models, however,
62 cannot accurately simulate observed transport of coarse dust particles across the Atlantic (Weinzierl et al., 2017;
63 Ansmann et al., 2017), although several hypotheses have been proposed to explain measurements of giant dust
64 particles (larger than 63 µm in diameter) relatively far from source regions (van der Does et al., 2018). For instance,
65 The potential mechanism for long-range transport of giant dust particles is that the uplift events of coarse dust can be
66 induced by a nocturnal low-level jet or cold pool outflow from mesoscale convective systems (i.e., haboobs)
67 (Rosenberg et al., 2014; Ryder et al., 2019). At higher elevation, electrostatic forces ~~and dust asphericity~~ might retard

68 the settling of coarse and giant dust particles and thus may facilitate the transport of these particles over longer
69 distances (Harrison et al., 2018; Toth et al., 2019; ~~Huang et al., 2020a~~). Other missing processes that affect the
70 transport and deposition of giant particles would also need to be incorporated into the models to reproduce the
71 measurements of the size distribution over the open ocean (van der Does et al., 2018). The coarse dust particles scatter
72 and absorb both the solar (~~short wave: SW~~) and thermal (~~long wave: LW~~) radiation, causing a net warming effect at
73 TOA. In contrast, the fine dust particles principally scatter SW radiation, causing a net cooling effect. Since coarse
74 dust tends to warm the climate, the underestimation of the abundance of coarse dust causes Earth system models to
75 underestimate the warming near the dust source regions. ~~On the other hand, model errors due to the underestimated~~
76 ~~coarse dust load and corresponding warming might be compensated for in models by using a refractive index that is~~
77 ~~too absorbing (Di Biagio et al., 2019, 2020), and which depends on the mineral composition of the dust.~~

78 ~~Second, The dust refractive index is often derived from measurements based on dust or individual mineral~~
79 ~~particles (Bedidi and Cervelle, 1993; Long et al., 1993; Di Biagio et al., 2017, 2019; Stegmann & Yang, 2017). Indeed,~~
80 ~~most dust particles are internal mixtures of various mineral compositions and irregular shapes (Reid, 2003; Wiegner~~
81 ~~et al., 2009; Wagner et al., 2012). In desert soils, iron (Fe) oxides are generally hematite (α -Fe₂O₃) and goethite~~
82 ~~(FeOOH), which cause soil derived dust absorption at ultraviolet (UV) and visible wavelengths (Sokolik and Toon,~~
83 ~~1999; Balkanski et al., 2007). These two minerals have distinct optical properties, which might cause various~~
84 ~~intensities of shortwave absorption and thus RE of dust aerosols (Lafon et al., 2016). However, the speciation of dust~~
85 ~~into its mineral components inherently comprises uncertainties on soil mineralogy, Fe content in mineral, and~~
86 ~~refractive index of Fe oxides, partly due to the differences in prescribed parameters. The atmospheric aging of Fe-~~
87 ~~containing aerosols can further modulate the optical properties of Fe oxides (Ito et al., 2018), while the photochemical~~
88 ~~transformation of Fe oxides from lithogenic sources due to atmospheric processing is relatively limited (< 10%),~~
89 ~~compared to pyrogenic sources (Ito et al., 2019).~~

90 ~~Previous studies have shown that the assumption of spherical shape in models leads to a substantial~~
91 ~~underestimation of the extinction efficiency and thus dust aerosol optical depth (DAOD), mainly because the~~
92 ~~assumption of sphericity causes an underestimation of the surface to volume ratio compared to aspherical dust (Kok~~
93 ~~et al., 2017; Hoshyaripour et al., 2019; Tuccella et al., 2019). Overall, the net-SW radiative effect of dust asphericity~~
94 on climate simulations is minor on a global scale, partly because the larger DAOD is compensated for by the larger
95 asymmetry parameter of aspherical dust, which reduces the amount of radiation scattered backward to space (Räisänen
96 et al., 2013; Colarco et al., 2014). Moreover, non-spherical calcium-rich dust particles can be converted to spherical
97 particles, due to heterogeneous reactions with nitrate and sulfate on these particles, especially over polluted regions
98 (Laskin et al., 2005; Matsuki et al., 2005). As the plumes move downwind to the oceans, the dust aerosols can be

99 aggregated with sea salt in the marine boundary layer, which leads to more spherical shapes and larger sizes (Zhang
100 and Iwasaka, 2004). However, the assumption of spherical shape in models leads to a substantial underestimation of
101 the extinction efficiency and thus DAOD near the strong source regions, mainly because the assumption of sphericity
102 causes an underestimation of the surface-to-volume ratio compared to aspherical dust (Kok et al., 2017, 2021;
103 Hoshyaripour et al., 2019; Tuccella et al., 2020). Radiative effect efficiency is often used for the evaluation of the
104 models and is defined as the gradient of a linear least squares fit applied to AOD and dust radiative effect at each two-
105 dimensional (2-D) grid box ($W \cdot m^{-2} AOD^{-1}$). Thus, the estimates of the dust radiative effect efficiency could be biased,
106 in part, due to large uncertainties associated with the spherical assumption on AOD retrieval (Zhou et al., 2020).

107 Third, the dust refractive index is often derived from measurements based on dust or individual mineral particles
108 (Bedidi and Cervelle, 1993; Long et al., 1993; Di Biagio et al., 2017, 2019; Stegmann & Yang, 2017). Indeed, most
109 dust particles are internal mixtures of various mineral compositions and irregular shapes (Reid, 2003; Wiegner et al.,
110 2009; Wagner et al., 2012). In desert soils, iron (Fe) oxides are generally hematite ($\alpha\text{-Fe}_2\text{O}_3$) and goethite (FeOOH),
111 which cause soil-derived dust absorption at ultraviolet (UV) and visible wavelengths (Sokolik and Toon, 1999;
112 Balkanski et al., 2007). These two minerals have distinct optical properties, which might cause various intensities of
113 SW absorption and thus RE of dust aerosols (Lafon et al., 2016). The dust complex refractive index in the LW also
114 depends on the particle mineralogical composition (Sokolik et al., 1998). Di Biagio et al. (2017) found a linear
115 relationship between the magnitude of the imaginary refractive index at 7.0, 9.2, and 11.4 μm and the mass
116 concentration of calcite and quartz absorbing at these wavelengths. However, the speciation of dust into its mineral
117 components inherently comprises uncertainties on soil mineralogy, mineral content in size-segregated dust particles,
118 and refractive index of mineral, partly due to the differences in prescribed parameters such as the particle size. The
119 atmospheric aging of Fe-containing aerosols can further modulate the optical properties of Fe oxides (Ito et al., 2018),
120 while the photochemical transformation of Fe oxides from lithogenic sources due to atmospheric processing is
121 relatively limited ($< 10\%$), compared to pyrogenic sources (Ito et al., 2019).

122 Here, we focus on the influence of the size-resolved abundance of aspherical dust on the aerosol radiative effects
123 in a coupled global chemical transport model (IMPACT) (Ito et al., 2020 and references therein) with a radiative
124 transfer module (RRTMG) (Iacono et al., 2008) ~~(i.e., default simulation)~~. We improve the accuracy of these
125 simulations by correcting the bias in size-resolved dust concentration with the Dust Constraints from joint
126 Observational-Modelling-Experimental analysis (DustCOMM) data set (Adebisi et al., 2020) ~~(i.e., improved~~
127 ~~simulation)~~, as well as by considering the aspherical shape (Huang et al., 2020a, 2020b). We then explore the
128 sensitivity to dust refractive index. ~~After evaluating the model outputs against semi-observation-based DAOD at 550~~
129 ~~nm ($DAOD_{550}$) and radiative effect efficiencies, the improved simulation suggests much less atmospheric radiative~~

130 ~~heating over the major source regions, compared to the default simulation (0.15 vs. 0.79 W m⁻² on a global scale).~~
131 ~~The term “semi-observation based” is used for DAOD₅₅₀ and dust radiative effect efficiency when the estimates are~~
132 ~~based on the combination of observations and models.~~

133 2 Methods

134 ~~Since most models underestimate the coarse dust load differently (Ansmann et al., 2017; Adebisi and Kok,~~
135 ~~2020), the sensitivity of dust radiative effects to optical properties in the present study might be considerably is also~~
136 ~~different from previous other studies. In our study, we regard “fine” and “coarse” dust as dust particles with a diameter~~
137 ~~less than 2.5 μm (i.e., PM_{2.5}) and between 2.5 and 20 μm, respectively. Here, we~~
138 ~~examined the dust radiative effects~~
139 ~~using seven-ten different numerical experiments that varied (1) the simulated dust concentration and their size~~
140 ~~distribution, (2) particle shape, and (3) mineralogical composition (Tables 1 and 2). Two experiments used the dust~~
141 ~~concentrations calculated from the forward-IMPACT model with the finer dust size (denoted as “IMPACT_{fine}”).~~
142 ~~Subsequently, the simulated dust concentration and the size distribution were adjusted to the semi-observationally-~~
143 ~~based concentrations (Adebisi and Kok, 2020) in the other eight experiments with the coarser dust size (denoted as~~
144 ~~“DustCOMM_{coarse}”). The term “semi-observationally-based” is used for DustCOMM, DAOD₅₅₀, and dust radiative~~
145 ~~effect efficiency when the estimates are based on the combination of observations and models. Five sensitivity~~
146 ~~experiments were handled in the RRTMG calculations performed with different refractive indices and hourly averaged~~
147 ~~aerosol concentrations with the two chemical transport model simulations of “IMPACT” and “DustCOMM”. The~~
148 ~~other three experiments were calculated from the model output with a post-processor. The default two simulations used~~
149 ~~the spherical assumption on the particle shape (denoted as “Sphere”), whereas the dust asphericity was considered in~~
150 ~~the other six-eight experiments (denoted as “Asphere”). We then examined different refractive indices for the dust~~
151 ~~mineralogy to represent the regional variations in refractive indices (denoted as “region”, “mMineral”, “DB17”,~~
152 ~~“DB19”, “V83”, or “Less SW”, “More LW_{absorption}”, “More SW”, and “Less LW”). These sensitivity simulations~~
153 ~~and their radiative effects are summarized in Tables 1 and 2, respectively, with more details below. In section 2.3, we~~
154 ~~describe the DustCOMM data set used to adjust (1) size-resolved abundance of dust concentration. In section 2.4, we~~
155 ~~describe the adjustment factor of (2) particle shape for spectral optical properties. In section 2.5, we describe~~
156 ~~differences in spectral refractive indices due to (3) different mineralogical compositions for the radiative flux~~
calculation.

157 2.1 Aerosol chemistry transport model

158 This study used the Integrated Massively Parallel Atmospheric Chemical Transport (IMPACT) model (Ito et
159 al., 2020 and references therein). Simulations were performed for the year ~~of~~ 2016, using a horizontal resolution of
160 $2.0^{\circ} \times 2.5^{\circ}$ for latitude by longitude and 47 vertical layers. The chemical transport model was driven by used the
161 Modern Era Retrospective analysis for Research and Applications 2 (MERRA-2) reanalysis meteorological data from
162 the National Aeronautics and Space Administration (NASA) Global Modeling and Assimilation Office (GMAO)
163 (Gelaro et al., 2017). The radiative feedback of the dust on the climate model simulation can be predicted by a separate
164 version of the model (Penner et al., 2018).

165 The model simulated the emissions, chemistry, transport, radiation, and deposition of major aerosol species,
166 including mineral dust, black carbon (BC), particulate organic matter (POM), sulfate, nitrate, ammonium, and sea
167 spray aerosols, and their precursor gases. Atmospheric processing of mineral dust aerosols, during transport, were
168 projected for four distinct aerosol size bins ($<1.26 \mu\text{m}$, $1.26\text{--}2.5 \mu\text{m}$, $2.5\text{--}5 \mu\text{m}$, and $5\text{--}20 \mu\text{m}$ of diameter). In this
169 version of the IMPACT model, two modes were used for sulfate aerosol (nuclei and accumulation mode), and two
170 moments were predicted within each mode (sulfate aerosol number and mass concentration) (Liu et al., 2015). The
171 surface coating of sulfate on dust aerosols occurred as a result of the condensation of sulfuric acid gas on their surfaces,
172 coagulation with sulfate aerosol, and formation in aqueous reactions within cloudy regions of the atmosphere (Liu et
173 al., 2015). The heterogeneous uptake of nitrate, ammonium, and water vapor by each aerosol for each size bin was
174 interactively simulated in the model following a hybrid dynamical approach (Feng and Penner, 2007). Five types of
175 aerosols (i.e., dust, nucleated sulfate, carbonaceous aerosols from fossil fuel combustion, carbonaceous aerosols from
176 biomass burning, and sea salt) were assumed to be externally mixed in each size bin for the computation of spectral
177 optical properties (Xu and Penner, 2012). Dust emissions were dynamically simulated using a physically-based
178 emission scheme (Kok et al., 2014; Ito and Kok, 2017) with the soil mineralogical map (Journet et al., 2014; Ito and
179 Shi, 2016). To derive atmospheric concentration of mineral composition for dust aerosol, “tagged” tracer was used
180 for each size-resolved mineral source. The direct emissions of dust weare evenly distributed in mixing ratio throughout
181 the planetary boundary layer. The global scaling factor of dust emission was determined from the comparison of the
182 model results with ground-based AOD measurements near the dust source regions prior to the adjustment to the
183 DustCOMM (Kok et al., 2014; Ito and Kok, 2017). In recent review papers, multi-model evaluations of aerosol iron
184 concentrations and their solubilities have been comprehensively summarized on global and regional scales
185 (Myriokefalitakis et al., 2018; Ito et al., 2021).

186 To improve the accuracy of our simulations of mineral dust, we made several upgrades to the on-line emission
187 and gravitational settling schemes used in Ito et al. (2020). The dust emissions were extremely sensitive to soil

188 moisture, and thus the bias was adjusted with satellite observations (Ito and Kok, 2017). However, the satellite
189 measurements were only available every other day, depending on location. The Soil Moisture Active Passive (SMAP)
190 Level-4 Soil Moisture data product addressed these limitations by merging the satellite observations into a numerical
191 model of the land surface water and energy balance while considering the uncertainty of the observations and model
192 estimates (Reichle et al., 2019). In this work, we utilized the 3-hourly data of soil moisture derived from the SMAP
193 for barren and open shrublands, separately (Reichle et al., 2018). To achieve this, we used the MODerate resolution
194 Imaging Spectroradiometer (MODIS) land cover map at 500 m resolution to calculate the fraction of barren and open
195 shrublands in each ground surface layer (Friedl et al., 2019)

196 Compared to the assumption on spherical shapes of aerosols, the dust asphericity increased aerodynamic drag
197 at a given volume and mass, and thus increased gravitational settling lifetime by about 20% (Huang et al., 2020a).
198 Here, we implemented a globally averaged asphericity factor of 0.87 (Huang et al., 2020a) to the gravitational settling
199 scheme for mineral dust. ~~Nevertheless~~ ~~Consequently~~, the lifetime of the dust aerosol for the largest-size bin in the
200 IMPACT model, even after accounting for asphericity (1.4 days for 5–20 μm of diameter), was significantly shorter
201 than an ensemble of model results (2.1 ± 0.3 days for the mass mean diameter of 8.3 μm) (Kok et al., 2017). The
202 impact of this underestimate of atmospheric lifetime is explored using the DustCOMM data set, as was summarized
203 in Table 2 (E3 – E4).

204 2.2 Integration of IMPACT and RRTMG

205 To improve the accuracy of our simulations of dust RE, we made upgrades to the radiative transfer calculations
206 (Ito et al., 2018 and references therein). In this study, we integrated the Rapid Radiative Transfer Model for GCMs
207 (RRTMG) online within the IMPACT model to calculate the radiative fluxes associated with atmospheric aerosols.
208 RRTMG is a radiative transfer code that calculates the SW and LW atmospheric fluxes (Iacono et al., 2008). Given
209 the size range of dust particles, scattering and absorption in the on-line model ~~were~~ described in terms of Mie
210 theory. Assuming homogeneous spherical particles, the spectral optical properties such as the mass extinction
211 coefficient, single scattering albedo, and asymmetry parameter were calculated using a look-up table as a function of
212 refractive index and size parameter (Xu and Penner, 2012). The impact of this spherical assumption is explored using
213 aspherical factor, as was summarized in Table 2 (E5 – E4).

214 The mineral dust particles were assumed to follow prescribed size distributions within each size bin (Liu et al.,
215 2015). In applying the look-up table, the size spectrum for mineral dust was divided into 30 sub bins (Wang and
216 Penner, 2009). As for the SW, the particle size increased with the uptake of sulfate, nitrate, ammonium, and water by
217 the aerosols (Xu and Penner, 2012). These coating materials were treated as internally mixed with dust aerosol in each

218 size bin and thus can reduce solar absorption of mineral dust. ~~As the LW scattering was not accounted for in the~~
219 ~~RRTMG, we used the adjustment factors of 1.18 ± 0.01 and 2.04 ± 0.18 for the dry particles at the surface and TOA~~
220 ~~(Dufresne et al., 2002), following Di Biagio et al. (2020) who noted that this adjustment was estimated for dust of~~
221 ~~diameter less than $10 \mu\text{m}$ and thus might be a lower approximation of the LW scattering by coarse dust. The larger~~
222 ~~adjustment factor at TOA reflects the fact that the upward LW radiation emitted from the ground surface can be~~
223 ~~reduced through scattering and absorption, compared to the surface.~~ Subsequently, these optical properties were used
224 by the RRTMG to calculate RE based on dust mixing ratio distributions in the IMPACT model. The dust RE was
225 estimated as the difference in the calculated radiative fluxes with all aerosols and with all aerosols except the dust
226 aerosols for each bin. As the LW scattering was not accounted for in the RRTMG, we multiplied the LW radiative
227 fluxes by the adjustment factors of 1.18 ± 0.01 and 2.04 ± 0.18 for the dry particles at the surface and TOA (Dufresne
228 et al., 2002), following Di Biagio et al. (2020). The larger adjustment factor at TOA reflects the fact that the upward
229 LW radiation emitted from the ground surface can be trapped through scattering and absorption compared to the
230 surface.

231 The broadband direct and diffuse albedos for both the UV visible and visible IR were specified from the hourly
232 MERRA-2. The surface emissivity was based on the hourly MERRA-2. Long-lived greenhouse gas concentrations
233 were obtained from historical greenhouse gas concentrations for climate models (Meinshausen et al., 2017). Water
234 vapor concentrations were specified according to the MERRA-2. Cloud optical properties were calculated based on
235 the liquid and ice visible optical depths from the MERRA-2, prescribing effective radii of $10 \mu\text{m}$ for water droplets
236 and $25 \mu\text{m}$ for ice particles, respectively (Gettelman et al., 2010; Heald et al., 2014).

237 **2.3 Description of DustCOMM dataset and sensitivity experiments to size-resolved dust concentration**

238 Dust Constraints from joint Observational-Modelling-experiMental analysis (DustCOMM) is a dataset of
239 three-dimensional (3-D) dust properties obtained by combining observational, experimental, and modeling constraints
240 on dust properties. While details can be found in Adebisi et al. (2020) and Adebisi and Kok (2020), we provide a
241 brief overview here. First, DustCOMM's constraint on the 3-D dust size distribution combines dozens of previously
242 published in-situ measurements of dust size distributions, taken during several field campaigns, with an ensemble of
243 climate model simulations. The framework used those in-situ measurements first to constrain the globally averaged
244 size distribution (Adebisi and Kok, 2020), which is used subsequently to ~~bias-adjustment~~ the bias in an ensemble of
245 six global model simulations (Adebisi et al., 2020). The constraints on dust size distribution ranges from $0.2 \mu\text{m}$ to
246 $20 \mu\text{m}$ in diameter, where a generalized analytical function describes the sub-bin distribution based on brittle
247 fragmentation theory (Kok, 2011). The second DustCOMM product --atmospheric dust mass loading -- combines

248 the constraints on dust size distribution with constraints on dust extinction efficiency and dust aerosol optical depth
249 (Adebisi et al., 2020). The constraints on dust extinction efficiency used the single-scattering database of Meng et al.
250 (2010) and leveraged measurements of the dust index of refraction as well as accounts for the non-spherical shape of
251 dust particles (Kok et al., 2017). For this, we approximate dust as tri-axial ellipsoidal particles described by the
252 globally-representative values of measured dust aspect ratio (the length-to-width ratio), and the height-to-width ratio
253 (HWR) obtained from Huang et al. (2020a). Furthermore, the dust aerosol optical depth used to obtain the dust mass
254 loading combines the semi-observationally-based dataset from Ridley et al. (2016) with information from four
255 reanalysis products. This includes the MERRA-2, Navy Aerosol Analysis and Prediction System (NAAPS), Japanese
256 Reanalysis for Aerosol (JRAero), and Copernicus Atmosphere Monitoring Service interim ReAnalysis (CAMSiRA)
257 (Adebisi et al., 2020).

258 The aerosol RE of mineral dust strongly depends on both the magnitude of dust load and the dust size
259 distribution (Tegen and Lacis, 1996; Liao and Seinfeld, 1998). The DustCOMM data set contains total column loading
260 and concentration of mineral dust resolved by season and particle size (Adebisi et al., 2020). To correct the bias in
261 the seasonally averaged size-resolved dust emission in the IMPACT model, the sum of bin 1, bin 2, and bin 3 dust
262 emission flux was scaled by the seasonal mean of the ratio of the sum of bin 1, bin 2, and bin 3 dust column loading
263 between the model and DustCOMM at each 2-D grid box. When the source function was used for high-latitude dust
264 in the Northern Hemisphere, this led to substantially high emissions and thus RE over there, likely due to the influences
265 from long-range transported dust. Therefore, the direct emissions of dust from the nine major source regions only
266 (Kok et al., 2021) were adjusted using the DustCOMM data (Fig. 1). To adjust the size bias in dust emissions, the
267 mass fraction of emitted dust for each bin was prescribed according to the size-resolved total column loading of
268 DustCOMM at each 2-D grid box. Overall, the IMPACT-simulated lifetime of the dust aerosol for the second-size bin
269 (7.8 days 1.26–2.5 μm of diameter) was in good agreement with the ensemble of model results (8.5 ± 1.1 days for the
270 mass mean diameter of 1.8 μm) (Kok et al., 2017). To correct the bias in the seasonally averaged 3-D dust size
271 distribution after the transport, the mass fraction of dust concentration for each bin between 0.2 and 20.0 μm of
272 diameter was scaled at each 3-D grid box prior to calculating the radiative fluxes using the RRTMG by the ratio of
273 mass concentration of $\text{PM}_{2.5}$ (i.e., the sum of bin 1 and bin 2) to each bin (Table 3).

274 **2.4 ~~Description of a~~ sphericity factor for optical properties and sensitivity experiments to particle shape**

275 To account for the dust asphericity, an adjustment factor was applied to the spherical optical properties at each
276 dust size parameter and refractive index. The adjustment factors for the spectral optical properties of non-spherical
277 particles were calculated after Huang et al. (2020b). The atmospheric aging of mineral dust can form a uniform coating

278 around the mineral core and therefore decrease particle asphericity during transport. This is implicitly considered in
279 the globally averaged shape distribution of dust (Huang et al., 2019). Specifically, Huang et al. (2020b) combined
280 globally representative dust shape distributions (Huang et al., 2020a) with a shape-resolved single-scattering database
281 (Meng et al., 2010). This database combines four computational methods (Mie theory, T-matrix method, discrete
282 dipole approximation, and an improved geometric optics method) to compute the single-scattering properties of non-
283 spherical dust for a wide range of shape descriptors. Huang et al. (2020b) provided the look-up table containing optical
284 properties of non-spherical dust as functions of size parameter and refractive index.

285 The approximation of particles to spheres is evaluated by applying aspherical factors to the optical properties
286 of the mass extinction coefficient, single scattering albedo, and asymmetry parameter for SW, as well as absorption
287 fraction of extinction for the LW. At the same time, we maintained the consideration of asphericity on the gravitational
288 velocity and kept the dust concentrations unaltered between the spherical (denoted as “Sphere”) and aspherical
289 (denoted as “Asphere”) cases.

290 **2.5 Spectral refractive index and sensitivity experiments to mineralogical compositions**

291 The aerosol RE of mineral dust depends on mineralogical composition. For the sensitivity simulation to the
292 SW and LW refractive indices, we used the global mean of laboratory measurements of the refractive index from 19
293 natural soils from various source regions around the world in Di Biagio et al. (2019) (denoted as “DB19”) and in Di
294 Biagio et al. (2017) (denoted as “DB17”), respectively. To illustrate the regional heterogeneity of refractive index, the
295 refractive index obtained from 19 samples was aggregated into 9 main source regions, and the arithmetic mean was
296 calculated for each source region (Di Biagio et al., 2017, 2019). The regionally averaged imaginary parts of the
297 refractive indices at the wavelength of 0.52 μm and 9.7 μm showed large differences in SW and LW absorptivity,
298 respectively, between different samples collected at various geographical locations (Fig. 1).

299 The optical properties from the measurements for dust samples generated from 19 natural soils suggested a
300 considerable role of Fe oxides in determining the SW absorption (Di Biagio et al., 2019). The refractive indices for
301 mineral components were used for hematite, goethite (Bedidi and Cervelle, 1993), silicate particle group, quartz,
302 gypsum (CaSO_4) (Stegmann & Yang, 2017), and calcite (CaCO_3) (Long et al., 1993) in the simulations denoted as
303 “Mineral”. The hematite and goethite were treated separately according to the mineralogical map (Journet et al., 2014).
304 Consequently, hematite mass content averaged in the dust at emission (0.79% for fine and 0.50% for coarse from the
305 IMPACT simulation) was lower than goethite content (1.8% and 1.3%, respectively) on a global scale. In addition to
306 the primary emission of gypsum, CaSO_4 is secondarily formed due to the dissolution/precipitation of CaCO_3 in
307 thermodynamic equilibrium condition (Ito and Feng, 2010). To illustrate the difference in refractive index, the global

308 mean of the mineral composition was used for the comparison with DB19 (Fig. 1). The imaginary parts of the
309 refractive indices from mineralogical map were higher than DB17, resulting in a stronger absorption over the SW
310 spectrum.

311 The mineral dust LW refractive index also depends on its mineralogical composition (Sokolik et al., 1998; Di
312 Biagio et al., 2017). The LW refractive index of Volz (1983) has been widely used in climate models and satellite
313 remote sensing algorithms and thus was examined here (denoted as “V83”) (Song et al., 2018). The imaginary parts
314 of the refractive indices from V83 were higher than DB19, resulting in a stronger absorption over most of the LW
315 spectrum. To analyze the dependence of the results on less (more) absorptive SW and less (more) absorptive LW
316 refractive indices, we made further sensitivity simulations by varying the values of imaginary parts of the refractive
317 index within the range of values from Di Biagio et al. (2017, 2019) (10% or 90% percentiles for SW or LW,
318 respectively) (denoted as “Less” or “More”). The associated real parts with 10% or 90% percentile imaginary parts
319 for LW were calculated to account for the Kramers-Kronig relation (Lucarini et al., 2005).

320 **2.5 — Sensitivity simulations**

321 ~~First, the aerosol RE of mineral dust strongly depends on both the magnitude of dust load and the dust size~~
322 ~~distribution (Tegen and Lacis, 1996; Liao and Seinfeld, 1998). The DustCOMM data set contains total column loading~~
323 ~~and concentration of mineral dust resolved by season and particle size (Adebisi et al., 2020). To adjust the seasonal~~
324 ~~dust load in the model, the sum of bin 1, bin 2, and bin 3 dust emission flux was scaled by the seasonal mean of the~~
325 ~~ratio of the sum of bin 1, bin 2, and bin 3 dust column loading between the model and DustCOMM at each 2-D grid~~
326 ~~box. When the source function was used for high latitude dust in the Northern Hemisphere, this led to substantially~~
327 ~~high emissions and thus RE over there, likely due to the influences from long range transported dust. Therefore, the~~
328 ~~direct emissions of dust from the nine major source regions only (Kok et al., 2020) were adjusted using the~~
329 ~~DustCOMM data (Fig. 1). To adjust the size bias in dust emissions, the mass fraction of emitted dust for each bin was~~
330 ~~prescribed according to the size resolved total column loading of DustCOMM at each 2-D grid box. Overall, the~~
331 ~~IMPACT simulated lifetime of the dust aerosol for the second size bin (7.8 days 1.26–2.5 μm of diameter) was in~~
332 ~~good agreement with the ensemble of model results (8.5 ± 1.1 days for the mass mean diameter of 1.8 μm) (Kok et~~
333 ~~al., 2017). To maintain the consistency in the DAOD₅₅₀, the mass fraction of dust concentration for each bin between~~
334 ~~0.2 and 20.0 μm of diameter were adjusted at each 3-D grid box prior to calculating the radiative fluxes using the~~
335 ~~RRTMG based on the ratio of mass concentration of PM_{2.5} (i.e., sum of bin 1 and bin 2) to each bin (Table 3).~~

336 ~~Second, the approximation of particles to spheres is evaluated applying aspherical factors to the optical~~
337 ~~properties of the mass extinction coefficient, single scattering albedo, and asymmetry parameter for SW, as well as~~

338 absorption fraction of extinction for the LW. At the same time, we maintained the consideration of asphericity on the
339 gravitational velocity and kept the dust concentrations unaltered between the spherical (default) and aspherical (fine-
340 global) cases.

341 Third, the aerosol RE of mineral dust also depends on mineralogical composition. For the sensitivity simulation
342 to refractive index, we used the global mean of laboratory measurements of the refractive index from 19 natural soils
343 from various source regions around the world (Di Biagio et al., 2017, 2019) (denoted as “global”). To investigate the
344 regional heterogeneity of refractive index, regional mean of refractive index was examined (denoted as “region”). The
345 regionally averaged imaginary parts of the refractive indices at wavelength of 0.52 μm and 9.7 μm showed large
346 differences in SW and LW absorptivity, respectively, between different samples collected at various geographical
347 locations (Fig. 1). The refractive index obtained from 19 samples was aggregated into 9 main source regions and the
348 arithmetic mean was calculated for each source region (Di Biagio et al., 2017, 2019). The global mean was used for
349 other areas. The mineral dust LW refractive index also depends on its mineralogical composition (Sokolik et al., 1998;
350 Di Biagio et al., 2017). The LW refractive index of Volz (1983) has been widely used in climate models and satellite
351 remote sensing algorithms and thus was examined here (denoted as “mineral”). To analyze the dependence of the
352 results on less absorptive SW and more absorptive LW refractive indices, we made further sensitivity simulations by
353 varying the values of imaginary parts of the refractive index within the range of values from Di Biagio et al. (2017,
354 2019) (10% and 90% percentiles for SW and LW, respectively) (denoted as “absorption”). The associated real parts
355 with the 90% percentile imaginary parts for LW were calculated to account for the Kramers-Kronig relation (Lucarini
356 et al., 2005).

357 2.6 Semi-observationally-based dust SW and LW radiative effect efficiency

358 Radiative effect efficiency is defined as the gradient of a linear least squares fit applied to the DAOD_{550} and
359 dust radiative effect at each 2-D grid box ($\text{W m}^{-2} \text{DAOD}_{550}^{-1}$). To estimate dust radiative effect efficiency, aerosol
360 and radiation remote sensing products have been used with various methods (Table 4) (Zhang and Christopher 2003;
361 Li et al. 2004; Christopher and Jones 2007; Brindley and Russell 2009; Yang et al. 2009; Di Biagio et al. 2010; Hansell
362 et al. 2010; Hansell et al. 2012; Song et al. 2018).

363 The instantaneous SW radiative effect efficiency at TOA is obtained from the linear regression of TOA
364 radiation flux versus AOD observations, although the values in low-dust periods can be substantially influenced by
365 other types of aerosols such as biomass burning (Li et al. 2004). This radiative effect efficiency corresponds to the
366 instantaneous value derived under the limited condition at the measurements (e.g., solar position, atmospheric

367 condition). From the extrapolation of the instantaneous value, the diurnal mean dust SW radiative effect efficiency at
368 the surface and TOA can be derived based on model calculations.

369 The LW radiative effect efficiency at TOA can be obtained from the linear regression of TOA radiation flux
370 versus AOD observations over the source regions (Brindley and Russell 2009). However, the observed outgoing
371 ~~longwave-LW~~ radiation is not only dependent on DAOD but also on other factors such as dust layer height, water
372 vapor content, and other types of aerosols. Thus, the LW radiative effect efficiency is estimated from the difference
373 between observed outgoing ~~longwave-LW~~ radiation and the dust-free outgoing ~~longwave-LW~~ radiation, which can be
374 estimated using radiative transfer model (Song et al., 2018).

375 Consequently, the semi-observation~~ally~~-based estimates of the dust radiative effect efficiency could be biased,
376 in part, due to large uncertainties associated with the estimation method ~~such as spherical assumption on AOD retrieval~~
377 ~~(Zhou et al., 2020)~~, the selection of cloud-free and dust-dominant data, and dust physicochemical properties. To
378 understand the sensitivity of the dust radiative effect efficiency to the particle size distribution, asphericity, and
379 refractive index of dust, radiative transfer computations have been carried out in previous studies (Li et al., 2004;
380 Song et al., 2018). Song et al. (2018) found that the combination of the coarser dust particle size distribution and the
381 more absorptive LW refractive index (V83) yielded the best simulation of the dust LW radiative effect in comparison
382 with the satellite flux observations (i.e., CERES), compared to the less absorptive LW refractive index (DB17).

383 3. Results and Discussions

384 We evaluate our results from ~~the~~ sensitivity simulations against semi-observation~~ally~~-based estimates of
385 DAOD₅₅₀ in section 3.1 and radiative effect efficiency for SW and LW in section 3.2 and section 3.3, respectively.
386 We focused this evaluation on the North Africa and the North Atlantic in boreal summer (June, July, and August)
387 partly because that ~~was-is~~ the region and season for which most observational constraints on dust radiative effects
388 ~~were-are~~ available. The better agreement is obtained for the less absorptive SW (Di Biagio et al., 2019) and the more
389 absorptive LW (Volz, 1983) dust refractive indices with adjustments of size-resolved dust concentration and particle
390 shape. Our improved simulation from IMPACT-Sphere-Mineral-V83 (E1) to DustCOMM-Asphere-DB19-V83 (E2)
391 substantially reduces the model estimates of atmospheric radiative heating ~~due to by~~ mineral dust near the major source
392 regions even though it induces only a minor difference in RE at TOA on a global scale (section 3.4), compared to the
393 default simulation. To elucidate the differences in dust radiative effects between different simulations, the results from
394 the sensitivity simulations in conjunction with previous modeling studies are analyzed in section 3.5.

3.1 Dust load and aerosol optical depth

We compared our model estimates of DAOD₅₅₀ against semi-observationally-based data in box plots and Taylor diagrams (Taylor, 2001) for the evaluation of the various model experiments against semi-observationally-based estimates (Ridley et al., 2016; Adebisi et al., 2020) to provide a concise statistical summary of the bias, correlation coefficient, root mean square errors, and the ratio of standard deviation (Fig. 2, Tables S1 and S2). Because assuming spherical dust underestimates the mass extinction efficiency by ~30% (Kok et al., 2017), IMPACT-Sphere-Mineral-V83 (E1) default simulations resulted in a significant underestimation of the global and annual mean of DAOD₅₅₀ (0.023) (Fig. 2 and Table 3). The lower DAOD₅₅₀ from E2 than E1 was mostly found over East Asia and Bodele/Sudan in winter (Fig. 32, Table S2). After considering the dust asphericity for spectral optical properties (fine-global), we adjusted IMPACT-simulated dust loads against the constraints on dust load constrains of from the DustCOMM data set. This adjustment led the simulated total dust load to increase from 25 Tg (E1 default) to 32 Tg (E2 improved simulation), which addressed the issue that of model underestimated the coarse dust underestimation and fine dust overestimation by the model portion (Fig. 32, Table 3). After all Consequently, the global and annual mean of DAOD₅₅₀ from DustCOMM-Asphere-DB19-V83 (E2) the improved simulation (0.029) fell within the range in the semi-observationally-based estimate (0.030 ± 0.005) (Ridley et al., 2016) (Table 3). We found that the agreement in the median with the semi-observationally-based estimate (0.127) s in summer was improved from IMPACT-Sphere-Mineral-DB17 (0.049) default to DustCOMM-Asphere-DB19-V83 (0.117) improved simulations, with the correlation coefficients (root mean square errors) increasing (decreasing) from 0.86 (0.08) to 0.91 (0.06), respectively (solid line within the box mark in Fig. 32d, Table S1, Fig. S1). We also found improvements over East Asia and Bodele/Sudan in winter the other three seasons (Table S2). The better agreement suggested that DustCOMM-Asphere-DB19-V83 (E2) the improved simulation was reasonably constrained by the DAOD₅₅₀ (Ridley et al., 2016; Adebisi et al., 2020).

3.2 Dust SW radiative effect efficiency

Modeled estimates of clear-sky dust SW radiative effect efficiencies ($W \cdot m^{-2} DAOD_{550}^{-1}$) at the surface (Table S3) and TOA (Table S4) were compared with estimates reported by regional studies based on satellite observations over the North Africa and the North Atlantic (Fig. 4). Comparisons for other regions and seasons were also presented included for SW in Figs. 4(g), 4(h), 4(i), and 4(j) S2. Sensitivity simulations demonstrated that the radiative effect efficiency strongly depended on the particle size, refractive index, and particle shape (Fig. 4 and Fig. S3). The adjustment of size-resolved dust concentration and shape with the same refractive index worsened agreement led to overestimates of the SW radiative effect efficiencies against semi-observationally-based data for the correlation

425 coefficients (root mean square errors) decreasing (increasing) from 0.96 (17) at TOA (from E1 default simulations) to
426 0.94 (26) (from E6 coarse mineral) (in Fig. S24h). Subsequently, the use of less absorptive SW refractive index with
427 DustCOMM-Asphere-DB19-V83 (E2) the improved simulations led to a better agreement for the correlation
428 coefficients (root mean square errors) increasing (decreasing) to 0.95 (22) (from the improved simulation) (from E6
429 to E2 in Fig. S24). However, On the other hand, the use of much less (10% percentile) absorptive SW refractive index
430 from DustCOMM-Asphere-Less-More (E7) coarse absorption simulation (Fig. S2e) deteriorated the agreement due to
431 the underestimate of cooling at the surface (Fig. 4g). In contrast, the use of a more absorptive SW refractive index
432 from DustCOMM-Asphere-Mineral-V83 (E6) improved the agreement at the surface. However, the semi-
433 observationally-based estimates of diurnally averaged radiative effect efficiency at the surface were derived from
434 extrapolation of the instantaneous values, which would affect the comparison due to differences in the methodologies
435 between dust models (section 2.6). The differences in the model-based estimates of radiative effect efficiency might
436 arise from different data sets of the refractive index, size distribution, and particle shape (Song et al., 2018).

437 3.3 Dust LW radiative effect efficiency

438 Modeled estimates of clear-sky dust LW (Fig. 5) radiative effect efficiencies ($\text{W} \cdot \text{m}^{-2} \text{DAOD}_{550}^{-1}$) at the surface
439 (Table S5) and TOA (Table S6) were compared with estimates reported by regional studies based on satellite
440 observations over North Africa and the North Atlantic. Comparisons for other regions and seasons were also
441 ~~presented~~ included for LW Figs. 5(g), 5(h), 5(i), and 5(j) S4. Sensitivity simulations demonstrated that the radiative
442 effect efficiency strongly depended on the particle size, refractive index, and particle shape (Fig. 5 and Fig. S5). ~~The~~
443 Both the IMPACT-Sphere-Mineral-V83 (E1) and DustCOMM-Asphere-DB19-V83 (E2) improved simulations
444 yielded better agreement with semi-observationally-based data at the surface and TOA, compared to the less
445 absorptive LW dust refractive indices, with the correlation coefficients (root mean square errors) increasing
446 (decreasing) from 0.57 (12) (from default simulation) to 0.58 (6.3) (from the improved simulation) (E3, E4, E5, and
447 E7) (Fig. S4). ~~Substantial differences in dust LW radiative effect efficiencies between the default and the improved~~
448 ~~simulations were found at the surface over the major source regions. The improved simulation showed better~~
449 ~~agreements with semi-observation based estimates of LW radiative effect efficiencies at the surface over tropical~~
450 ~~Atlantic (21 vs. 24 $\text{W} \cdot \text{m}^{-2} \text{DAOD}^{-1}$) and China (33 vs. 31–35 $\text{W} \cdot \text{m}^{-2} \text{DAOD}^{-1}$) compared to the default simulation~~
451 ~~(8.8 and 22 $\text{W} \cdot \text{m}^{-2} \text{DAOD}^{-1}$, respectively).~~ The relatively high LW radiative effect efficiencies over western Africa
452 were also consistent with the semi-observationally-based data. On the other hand, the relatively low LW radiative
453 effect efficiencies were found over eastern Africa. Moving toward the northeastern side of the region, however, the
454 associated uncertainties in the semi-observationally-based values increased (Brindley and Russell 2009). The dust LW

radiative effect efficiency depends strongly on the vertical profile of dust concentration, temperature, and water vapor, which would affect the comparison due to a high variability in these factors (section 2.6).

3.45 Atmospheric Dust radiative heating effect by dust due to coarser size and aspherical shape

The Saharan dust cools the ground surface by reducing the solar radiation reaching the surface and warms the atmosphere by absorbing solar radiation (Fig. 6). On the other hand, thermal emission by dust warms the surface and cools the atmosphere (Fig. 7). Our sensitivity simulations showed that the annually averaged net instantaneous radiative effect due to mineral aerosol (NET) ranged from -0.438 (~~DustCOMM-Asphere-Less-Less-coarse-absorption~~) to $+0.25$ (~~DustCOMM-Asphere-Mineral-V83-coarse-mineral~~) $\text{W}\cdot\text{m}^{-2}$ at TOA (Table 5). The net RE from both the ~~IMPACT-Sphere-Mineral-V83~~ ($-0.00 \text{ W}\cdot\text{m}^{-2}$) ~~default~~ and ~~DustCOMM-Asphere-DB19-V83~~ ($-0.08 \text{ W}\cdot\text{m}^{-2}$) ~~improved~~ simulations resulted within similar NET RE (-0.09 and $-0.08 \text{ W}\cdot\text{m}^{-2}$, respectively) to ~~98% confidential interval of DustCOMM data set~~ (-0.1127 to $0.104 \text{ W}\cdot\text{m}^{-2}$).

The SW RE by dust outweighs the ~~longwave-LW~~ warming effect at the surface in the ~~default-IMPACT-Sphere-Mineral-V83 (E1)~~ simulation (Fig. 8). Consequently, the highly absorbing dust could play an important role in the aerosol radiative forcing for the climate models to alter the West African monsoon, with the radiative heating concentrated in the dust layer (Miller et al., 2004b; Lau et al., 2009). Our model results of dust RE from ~~DustCOMM-Asphere-DB19-V83 (E2)~~ ~~improved~~ simulation, however, suggested that the surface warming was substantially enhanced near the strong dust source regions ~~much less cooling~~ ($-0.23 \text{ W}\cdot\text{m}^{-2}$ ~~on a global scale~~) ~~at the surface~~ (Fig. 8), compared to the ~~V83 default~~ simulation ($-0.6088 \text{ W}\cdot\text{m}^{-2}$ ~~on a global scale~~), ~~despite similar RE at TOA on a global scale~~. Thus, our results demonstrated that the atmospheric radiative heating ~~due to by~~ mineral dust was substantially reduced for ~~DustCOMM-Asphere-DB19-V83 (E2)~~ ~~the improved~~ simulation ($0.15 \text{ W}\cdot\text{m}^{-2}$), compared to the ~~IMPACT-Sphere-Mineral-V83 (E1)~~ ~~default~~ simulation ($0.759 \text{ W}\cdot\text{m}^{-2}$). ~~The improved simulation was obtained from the evaluation against semi-observation based estimates of DAOD₅₅₀, SW₁ and LW radiative effect efficiencies.~~

3.5 Synergy of coarser size and aspherical shape

To ~~investigate-elucidate~~ the differences in dust radiative effects between the ~~IMPACT-Sphere-Mineral-V83 (E1) default~~ and ~~DustCOMM-Asphere-DB19-V83 (E2)~~ ~~improved~~ simulations (Fig. 9), the differences in annually averaged radiative effects of mineral dust from ~~DustCOMM-Asphere-DB19-DB17 (E4)~~ ~~coarse-global~~ simulation were shown in Fig. 109. A slope of one in Fig. 109 represented an identical change in both the surface and TOA, and thus corresponded to no change in radiative heating within the atmosphere. The distances from the ~~DustCOMM-Asphere-DB19-DB17 (E4)~~ ~~coarse-global~~ simulation demonstrated that the large uncertainties existed for the size distribution

484 and spectral optical properties refractive index. Our sensitivity simulations revealed that the DustCOMM-Asphere-
485 DB19-V83 (E2) ~~the improved~~ simulation led to a similar enhancement of NET_{net} RE at TOA to the IMPACT-Sphere-
486 Mineral-V83 (E1) ~~default~~ simulation (+0.12 vs. +0.11 W·m⁻² at the vertical axis of red star and black star, respectively,
487 in Fig. 9e) but ~~resulted~~ led in less cooling at the surface (+0.42 vs. -0.20 W·m⁻² at the horizontal axis in Fig. 9e) (Fig.
488 9). This revision can be divided into (1) the size-resolved abundance for both SW and LW (black triangles hexagons
489 in Fig. 10 in Fig. 109a and Fig. 910b, respectively), (2) mineralogical variability refractive index for SW (red diamonds
490 in Fig. 9a) and for LW (red diamonds and triangle in Fig. 9b), and (3) particle shape (red circles).

491 First, at TOA, the SW RE was more sensitive to the size-resolved abundance (-0.17 W·m⁻² at the vertical axis
492 of black hexagon triangle in Fig. 109a), compared to LW (0.04 W·m⁻² at the vertical axis of black hexagon triangle
493 in Fig. 109b) (Liao and Seinfeld, 1998). Second, this less SW cooling effect with coarser dust was partially
494 compensated for by more SW cooling by the less absorptive SW refractive index (0.343 W·m⁻² at the vertical axis of
495 red diamond in Fig. 109a). Thirdly, the sensitivity of SW RE to dust asphericity was rather minor (0.04 W·m⁻² at the
496 vertical axis of red circle in Fig. 10a), partly because the lower DAOD was compensated for by the lower asymmetry
497 parameter of spherical dust, which enhanced the amount of radiation scattered backward to space (Räisänen et al.,
498 2013; Colarco et al., 2014). The partial compensation led to a small enhancement of SW RE for the IMPACT-Sphere-
499 Mineral-V83 (E1) ~~default~~ simulation (-0.13 W·m⁻² at the vertical axis of black star in Fig. 9a) and thus the resulting
500 similar NET_{net} RE to DustCOMM-Asphere-DB19-V83 (E2) at TOA (Fig. 9e).

501 In contrast, at the surface, our sensitivity simulations demonstrated substantially different responses in the RE,
502 mostly because of LW warming effects (+0.42 vs. -0.20 W·m⁻² at the horizontal axis in Fig. 109b). The enhanced
503 SW cooling by the more absorbing dust (-0.38 W·m⁻² at the horizontal axis of red diamond in Fig. 9a) was mostly
504 compensated for by the reduced SW cooling with coarser dust (0.12 W·m⁻² at the horizontal axis of black triangle in
505 Fig. 9a) and asphericity. This led to minor change in SW cooling by the default simulation (-0.03 W·m⁻² at the
506 horizontal axis of black star in Fig. 9a). In contrast, enhanced LW warming by coarser dust (-0.08 W·m⁻² at the
507 horizontal axis of black hexagon in Fig. 10b) more absorptive LW refractive index (+0.42 W·m⁻² at the horizontal axis
508 of red diamond in Fig. 9b) was accompanied with enhanced LW warming by the coarser dust (0.07 W·m⁻² at the
509 horizontal axis of black triangle in Fig. 9b) and asphericity (-0.153 W·m⁻² at the horizontal axis of red circle from the
510 difference between black triangle and black star in Fig. 109b), because the enhancement of the absorption fraction of
511 extinction due to asphericity was larger at coarser size. This enhanced LW warming effects of each as well as the
512 synergy was further amplified using the more absorptive LW dust refractive index (Volz, 1983) (at the horizontal axis
513 of red diamond in Fig. 10b). As a result, our sensitivity simulations revealed that substantially less dust absorption at
514 LW due to the underestimation of the coarse dust load and the assumption of the spherical shape (IMPACT-Sphere-

515 Mineral-V83) contributed to the less surface warming~~the reduced radiative heating within the atmosphere, compared~~
516 to DustCOMM-Asphere-DB19-V83 (Fig. 9)~~(less than the dashed line of red star in Fig. 9c) by the improved~~
517 simulation ($-0.30 \text{ W}\cdot\text{m}^{-2}$), compared to the enhanced radiative heating (more than the dashed line of black star in Fig.
518 9c) by default simulation ($0.34 \text{ W}\cdot\text{m}^{-2}$).

519 A relatively good agreement of net RE by dust at TOA with Di Biagio et al. (2020) ($-0.06 \text{ W}\cdot\text{m}^{-2}$) could be
520 obtained from both the IMPACT-Sphere-Mineral-V83 (E1) and DustCOMM-Asphere-DB19-V83 (E2) simulations
521 (Fig. 9 and Table 5). On the other hand, our modeled dust net RE at the surface from DustCOMM-Asphere-DB19-
522 V83 (E2) was much larger than Di Biagio et al. (2020) ($-0.63 \text{ W}\cdot\text{m}^{-2}$) and IMPACT-Sphere-Mineral-V83 (E1). The
523 synergy of coarser size and aspherical dust could contribute to the less surface warming of the DustCOMM-Asphere-
524 DB19-V83 (E2). At the same time, the more absorptive LW dust refractive index (V83) than DB17 (red diamond in
525 Fig. 10b) could also contribute to the less surface warming, which might be partially compensated for in our model
526 by the omission of dust with diameters in excess of $20 \mu\text{m}$. Consequently, our estimate of atmospheric radiative heating
527 by dust from DustCOMM-Asphere-DB19-V83 (E2) was lower than Di Biagio et al. (2020) ($0.63 \text{ W}\cdot\text{m}^{-2}$) and
528 IMPACT-Sphere-Mineral-V83 (E1). Additionally, the hot and dry climate over brighter desert surface exaggerates
529 differences in RE at the surface between the models (Miller et al., 2014). The low humidity allows dust particles to
530 absorb LW radiation with reduced competition from water vapor, while high temperatures within the boundary layer
531 increase downward thermal emission by dust (Liao and Seinfeld, 1998). The reduction of fine dust load after the
532 adjustment leads to underestimates of the SW cooling at TOA. To improve agreement against semi-observationally-
533 based estimate of the radiative effect efficiency at TOA, the less absorptive SW dust refractive index is required for
534 coarser aspherical dust. Thus, uncertainties in the size-resolved dust concentration, particle shape, and refractive index
535 contribute to the diversity in the simulated dust RE at the surface.

536 **4. Conclusions**

537 Accurate estimates of the size-resolved dust abundance, their spectral optical properties, and their seasonality
538 in regional and vertical scales provides a step towards a more reliable projection of the climatic feedback of mineral
539 aerosols. The radiative effect efficiency depends on numerous variables in model simulations, including the spatial
540 distribution and temporal variation of size-resolved dust concentrations, the mass extinction coefficient, single
541 scattering albedo, and asymmetry parameter of dust. Since the models typically underestimate the coarse dust load
542 and overestimate the fine dust load, the sensitivity to the aerosol absorptivity might be considerably different from
543 previous studies. Thus, the model results should be re-evaluated against semi-observationally-based estimate of the
544 DAOD₅₅₀ and dust radiative effect efficiency.

545 We improved the accuracy of the simulations by adjusting the bias in size-resolved aspherical dust
546 concentration with the DustCOMM data set. Alternatively, dust mineralogy might contribute to the underestimationes
547 of modeled aerosol absorption compared to satellite observations (Lacagnina, et al., 2015). This enhanced aerosol
548 absorption was examined by specifying the mineralogy with varying amounts of light-absorbing Fe oxides for SW.
549 The better agreement with the semi-observationally-based data of dust radiative effect efficiency was obtained using
550 the less absorptive SW and the more absorptive LW dust refractive indices after the adjustments of dust sizes and
551 shapes.

552 The diversity of modeled dust net RE at the surface ($-1.74 \text{ W}\cdot\text{m}^{-2}$ to $-0.20 \text{ W}\cdot\text{m}^{-2}$) is much larger than at TOA
553 ($-0.01 \text{ W}\cdot\text{m}^{-2}$ to $-0.61 \text{ W}\cdot\text{m}^{-2}$), partly because the refractive index is optimized to obtain reasonable agreement against
554 satellite observations of TOA radiation flux (e.g., CERES). The uncertainties in the size-resolved dust concentration,
555 particle shape, and refractive index contribute to the model diversity at the surface. DustCOMM-Asphere-DB19-V83
556 (E2)The improved simulation led to similar net global dust radiative effect at TOA on a global scale to IMPACT-
557 Sphere Mineral (E1)the default simulation (-0.08 vs. $-0.009 \text{ W}\cdot\text{m}^{-2}$) but resulted in less cooling at the surface by
558 the synergy of coarser size and aspherical shape, compared to IMPACT-Sphere-Mineral-V83 (E1) simulation (-0.23
559 vs. $-0.88 \text{ W}\cdot\text{m}^{-2}$ on a global scale). Consequently, the atmospheric heating due to mineral dust was substantially
560 reduced for the DustCOMM-Asphere-DB19-V83 (E2) improved simulation ($0.15 \text{ W}\cdot\text{m}^{-2}$), compared to the intensified
561 atmospheric heating from the IMPACT-Sphere-Mineral-V83 (E1)default IMPACT simulation ($0.759 \text{ W}\cdot\text{m}^{-2}$). The
562 less intensified atmospheric heating due to mineral dust could substantially modify the vertical temperature profile in
563 Earth system models, and thus has important implications for the projection of dust feedback near the major source
564 regions in the past and future climate changes (Kok et al., 2018). More accurate estimates of semi-observationally-
565 based dust SW and LW radiative effect efficienciesy over strong dust source regions are needed to narrow the
566 uncertainty in the RE.

567 Currently, the model did not include dust particles above $20 \mu\text{m}$, but a substantial fraction of airborne dust near
568 source regions may be above this threshold (Ryder et al., 2019). Moreover, such large particles can be transported to
569 higher altitudes and longer distances than the model prediction. The higher the dust layer resides, the larger the dust
570 LW RE at TOA is estimated under the clear-sky conditions (Liao and Seinfeld, 1998). Marine sediment traps, which
571 are located underneath the main Saharan dust plume in the Atlantic Ocean, suggest that giant particles are dominated
572 by platy mica and rounded quartz particles (van der Does et al., 2016). Thus, mineral composition of the giant particles
573 could be different from the aerosol samples generated from soils in the laboratory by Di Biagio et al. (2017), which
574 may reflect less absorbing LW refractive index of DB17 than V83. Indeed, the dust sample was collected for V83
575 from rainwater after strong wind. On the other hand, the contribution of the LW scattering might be underestimated

576 [in the models](#), as Di Biagio et al. (2020) noted that the adjustment factor was estimated for dust of diameter less than
577 [10 \$\mu\text{m}\$ and thus might be a lower approximation of the LW scattering by coarse dust. Therefore, a better understanding](#)
578 [of the effect of such large particles beyond 20 \$\mu\text{m}\$ and mineralogical composition on radiation balance remains a topic](#)
579 [of active research, given their potential to amplify the warming of the climate system](#). In such an extreme case as the
580 “Godzilla” dust storm over [the North Africa and the tropical Atlantic](#) in June 2020 (Francis et al., 2020), the dust
581 loading could be larger than that examined for this study, and our estimates of the warming effects might be
582 conservative during such events. However, to keep the giant particles in the atmosphere, the modeled deposition fluxes
583 should be reduced from the current model. Therefore, models should improve their ability to capture the evolution of
584 the dust size distribution as the plumes move downwind of the source regions.

585 **Code availability.**

586 The source code of the RRTMG has ~~ve~~ been obtained from the [website web site](#) at [https://github.com/AER-](https://github.com/AER-RC/RRTMG_LW)
587 [RC/RRTMG_LW](https://github.com/AER-RC/RRTMG_SW) and https://github.com/AER-RC/RRTMG_SW. The source code of the Kramers-Kronig relations
588 has ~~ve~~ been obtained from the [website web site](#) at [https://www.mathworks.com/matlabcentral/fileexchange/8135-tools-](https://www.mathworks.com/matlabcentral/fileexchange/8135-tools-for-data-analysis-in-optics-acoustics-signal-processing)
589 [for-data-analysis-in-optics-acoustics-signal-processing](https://www.mathworks.com/matlabcentral/fileexchange/8135-tools-for-data-analysis-in-optics-acoustics-signal-processing). [The source code of the Taylor diagram has been obtained](#)
590 [from the web site at https://www.mathworks.com/matlabcentral/fileexchange/20559-taylor-diagram](#).

591 **Data availability.**

592 SMAP data have been obtained from the [website web site](#) at <https://nsidc.org/data/smap/smap-data.html>. MODIS land
593 data have been retrieved from the [website web site](#) at <https://ladsweb.modaps.eosdis.nasa.gov/>. MERRA-2 data have
594 been provided by the Global Modeling and Assimilation Office (GMAO) at NASA Goddard Space Flight Center
595 (<https://disc.gsfc.nasa.gov/datasets/>). The DustCOMM data are available at <https://dustcomm.atmos.ucla.edu/>. The
596 datasets supporting the conclusions of this article are included within the article and its supplement file.

597 **Supplement.**

598 The supplement related to this article is available online at:

599 **Author contributions.**

600 AI and JFK initiated the modeling collaboration with semi-observation~~ally~~-based data sets. AI carried out the
601 modeling study. AAA, YH, JFK contributed semi-observation~~ally~~-based data sets of DustCOMM and asphericity
602 factor. All authors read and approved the final manuscript.

603 **Competing interests.**

604 The authors declare that they have no competing interests.

605 **Acknowledgements.**

606 Numerical simulations were performed using the Hewlett Packard Enterprise (HPE) Apollo at the Japan Agency for
607 Marine-Earth Science and Technology (JAMSTEC).

608 **Financial support.**

609 Support for this research was provided to A.I. by JSPS KAKENHI Grant Number 20H04329 and 18H04143, and
610 Integrated Research Program for Advancing Climate Models (TOUGOU) Grant Number JPMXD0717935715 from
611 the Ministry of Education, Culture, Sports, Science and Technology (MEXT), Japan. This work was developed with
612 support from the University of California President's Postdoctoral Fellowship awarded to A.A.A., and from the
613 National Science Foundation (NSF) grants 1552519 and 1856389 awarded to J.F.K. Y.H. acknowledges support from
614 NASA grant 80NSSC19K1346, awarded under the Future Investigators in NASA Earth and Space Science and
615 Technology (FINESST) program.

616 Review statement.

617 This paper was edited by and reviewed by two anonymous referees.

618 **References**

- 619 Adebisi, A. A., Kok, J. F., Wang, Y., Ito, A., Ridley, D. A., Nabat, P., and Zhao, C.: Dust Constraints from joint
620 Observational-Modelling-experiMental analysis (DustCOMM): comparison with measurements and model
621 simulations, *Atmos. Chem. Phys.*, 20, 829–863, <https://doi.org/10.5194/acp-20-829-2020>, 2020.
- 622 Adebisi, A. A. and Kok, J. F.: Climate models miss most of the coarse dust in the atmosphere, *Sci. Adv.*, 6, eaaz9507,
623 <https://doi.org/10.1126/sciadv.aaz9507>, 2020.
- 624 Albani, S., Mahowald, N. M., Perry, A. T., Scanza, R. A., Heavens, N. G., Zender, C. S., Maggi, V., Kok, J. F., and
625 Otto-Bliesner, B. L.: Improved dust representation in the Community Atmosphere Model. *J. Adv. Model.*
626 *Earth Syst.*, 6, 541–570, <https://doi.org/10.1002/2013MS000279>, 2014.
- 627 Ansmann, A., Rittmeister, F., Engelmann, R., Basart, S., Jorba, O., Spyrou, C., Remy, S., Skupin, A., Baars, H., Seifert,
628 P., Senf, F., and Kanitz, T.: Profiling of Saharan dust from the Caribbean to western Africa – Part 2:

629 Shipborne lidar measurements versus forecasts, *Atmos. Chem. Phys.*, 17, 14987–15006,
630 <https://doi.org/10.5194/acp-17-14987-2017>, 2017.

631 Balkanski, Y., Schulz, M., Claquin, T., and Guibert, S.: Reevaluation of Mineral aerosol radiative forcings suggests a
632 better agreement with satellite and AERONET data, *Atmos. Chem. Phys.*, 7, 81–95,
633 <https://doi.org/10.5194/acp-7-81-2007>, 2007.

634 Bedidi, A. and Cervelle, B.: Light scattering by spherical particles with hematite and goethitelike optical properties:
635 effect of water impregnation, *J. Geophys. Res.*, 98, 11941–11952, 1993, <https://doi.org/10.1029/93JB00188>.

636 Brindley, H. E. and Russell, J. E.: An assessment of Saharan dust loading and the corresponding cloud-free longwave
637 direct radiative effect from geostationary satellite observations, *J. Geophys. Res.-Atmos.*, 114, D23201, ~~2009~~,
638 <https://doi.org/10.1029/2008jd011635>, 2009.

639 Colarco, P. R., Nowottnick, E. P., Randles, C. A., Yi, B. Q., Yang, P., Kim, K. M., Smith, J. A., and Bardeen, C. G.:
640 Impact of radiatively interactive dust aerosols in the NASA GEOS-5 climate model: Sensitivity to dust
641 particle shape and refractive index, *J. Geophys. Res.-Atmos.*, 119, 753–786, ~~2014~~,
642 <https://doi.org/10.1002/2013JD020046>, 2014.

643 Christopher, S. A. and Jones, T.: Satellite-based assessment of cloud-free net radiative effect of dust aerosols over the
644 Atlantic Ocean, *Geophys. Res. Lett.*, 34, L02810, ~~2007~~, doi:10.1029/2006GL027783, 2007.

645 Di Biagio, C., di Sarra, A., and Meloni, D.: Large atmospheric shortwave radiative forcing by Mediterranean aerosol
646 derived from simultaneous ground-based and spaceborne observations, and dependence on the aerosol type
647 and single scattering albedo, *J. Geophys. Res.*, 115, D10209, ~~2010~~, <https://doi.org/10.1029/2009JD012697>,
648 2010.

649 Di Biagio, C., Formenti, P., Balkanski, Y., Caponi, L., Cazaunau, M., Pangui, E., Journet, E., Nowak, S., Caquineau,
650 S., Andreae, M. O., Kandler, K., Saeed, T., Piketh, S., Seibert, D., Williams, E., and Doussin, J.-F.: Global
651 scale variability of the mineral dust long-wave refractive index: a new dataset of in situ measurements for
652 climate modeling and remote sensing, *Atmos. Chem. Phys.*, 17, 1901–1929, ~~2017~~,
653 <https://doi.org/10.5194/acp-17-1901-2017>, 2017.

654 Di Biagio, C., Formenti, P., Balkanski, Y., Caponi, L., Cazaunau, M., Pangui, E., Journet, E., Nowak, S., Andreae, M.
655 O., Kandler, K., Saeed, T., Piketh, S., Seibert, D., Williams, E., and Doussin, J.-F.: Complex refractive
656 indices and single-scattering albedo of global dust aerosols in the shortwave spectrum and relationship to
657 size and iron content, *Atmos. Chem. Phys.*, 19, 15503–15531, ~~2019~~, [https://doi.org/10.5194/acp-19-15503-](https://doi.org/10.5194/acp-19-15503-2019)
658 2019, 2019.

659 Di Biagio, C., Balkanski, Y., Albani, S., Boucher, O., and Formenti, P.: Direct radiative effect by mineral dust aerosols
660 constrained by new microphysical and spectral optical data. *Geophys. Res. Lett.*, 47, e2019GL086186, ~~2020~~,
661 <https://doi.org/10.1029/2019GL086186>, ~~2020~~.

662 Dufresne, J., Gautier, C., Ricchizzi, P., and Fouquart, Y.: Longwave scattering effects of mineral aerosols, *J. Atmos.*
663 *Sci.*, 59(12), 1959–1966, 2002, [https://doi.org/10.1175/1520-0469\(2002\)059<1959:LSEOMA>2.0.CO;2](https://doi.org/10.1175/1520-0469(2002)059<1959:LSEOMA>2.0.CO;2).

664 [Feng, Y. and Penner, J. E.: Global modeling of nitrate and ammonium: Interaction of aerosols and tropospheric](#)
665 [chemistry, *J. Geophys. Res.*, 112, D01304, doi:10.1029/2005JD006404, 2007.](#)

666 Francis, D., Fonseca, R., Nelli, N., Cuesta, J., Weston, M., Evan, A., and Temimi, M.: The atmospheric drivers of the
667 major Saharan dust storm in June 2020. *Geophys. Res. Lett.*, 47, e2020GL090102, ~~2020~~,
668 <https://doi.org/10.1029/2020GL090102>, ~~2020~~.

669 Friedl, M., and Sulla-Menashe, D.: MCD12Q1 MODIS/Terra+Aqua Land Cover Type Yearly L3 Global 500m SIN
670 Grid V006 [Data set]. NASA EOSDIS Land Processes DAAC, ~~2019~~,
671 <https://doi.org/10.5067/MODIS/MCD12Q1.006>, ~~2019~~.

672 Gelaro, R., McCarty, W., Suárez, M. J., Todling, R., Molod, A., Takacs, L., Randles, C. A., Darmenov, A., Bosilovich,
673 M. G., Reichle, R., Wargan, K., Coy, L., Cullather, R., Draper, C., Akella, S., Buchard, V., Conaty, A., da
674 Silva, A. M., Gu, W., Kim, G.-K., Koster, R., Lucchesi, R., Merkova, D., Nielsen, J. E., Partyka, G., Pawson,
675 S., Putman, W., Rienecker, M., Schubert, S. D., Sienkiewicz, M., and Zhao, B.: The Modern-Era
676 Retrospective Analysis for Research and Applications, Version 2 (MERRA-2), *J. Climate*, 30, 5419–5454;
677 ~~2017~~, <https://doi.org/10.1175/JCLI-D-16-0758.1>, ~~2017~~.

678 Gettelman, A., Liu, X., Ghan, S. J., Morrison, H., Park, S., Conley, A. J., Klein, S. A., Boyle, J., Mitchell, D. L., and
679 Li, J. L. F.: Global simulations of ice nucleation and ice supersaturation with an improved cloud scheme in
680 the Community Atmosphere Model, *J. Geophys. Res.*, 115, D18216, ~~2010~~,
681 <https://doi.org/10.1029/2009jd013797>, ~~2010~~.

682 Harrison, R. G., Nicoll, K. A., Marlton, G. J., Ryder, C. L., and Bennett, A. J.: Saharan dust plume charging observed
683 over the UK, *Environ. Res. Lett.*, 13, 054018, <https://doi.org/10.1088/1748-9326/aabcd9>, 2018.

684 Hansell, R. A., Tsay, S., Hsu, N. C., Ji, Q., Bell, S.W., Brent, N. H., Welton, E. J., Roush, T. L., Zhang, W., Huang,
685 J., Li Z. Q., and Chen, H.: An assessment of the surface longwave direct radiative effect of airborne dust in
686 Zhangye, China, during the Asian Monsoon Years field experiment (2008), *J. Geophys. Res.*, 117, D00K39,
687 ~~2012~~, <https://doi.org/10.1029/2011JD017370>, ~~2012~~.

688 Hansell, R. A., Tsay, S. C., Ji, Q., Hsu, N. C., Jeong, M. J., Wang, S. H., Reid, J. S., Liou, K. N., and Ou, S. C.: An
689 assessment of the surface longwave direct radiative effect of airborne saharan dust during the NAMMA field
690 campaign, *J. Atmos. Sci.* 67, 1048–1065, ~~2010~~, doi:10.1175/2009JAS3257.1, [2010](#).

691 Heald, C. L., Ridley, D. A., Kroll, J. H., Barrett, S. R. H., Cady-Pereira, K. E., Alvarado, M. J., and Holmes, C. D.:
692 Contrasting the direct radiative effect and direct radiative forcing of aerosols, *Atmos. Chem. Phys.*, 14, 5513–
693 5527, ~~2014~~, <https://doi.org/10.5194/acp-14-5513-2014>, [2014](#).

694 Huang, Y., Kok, J. F., Kandler, K., Lindqvist, H., Nousiainen, T., Sakai, T., Adebisi, A., and Jokinen, O.: Climate
695 Models and Remote Sensing Retrievals Neglect Substantial Desert Dust Asphericity, *Geophys. Res. Lett.*,
696 47, e2019GL086592, ~~2020a~~, <https://doi.org/10.1029/2019GL086592>, [2020a](#).

697 Huang, Y., Adebisi, A., ~~&-and~~ Kok, J. 2020b, Linking the different diameter types of aspherical desert dust indicates
698 that models underestimate coarse dust emission, American Geophysical Union, Fall Meeting 2020, abstract
699 A007-0016, doi: 10.1002/essoar.10504925.1.

700 Hoshyaripour, G. A., Bachmann, V., Förstner, J., Steiner, A., Vogel, H., Wagner, F., Walter, C., and Vogel, B.: Effects
701 of Particle Nonsphericity on Dust Optical Properties in a Forecast System: Implications for Model-
702 Observation Comparison, *J. Geophys. Res.-Atmos.*, 124, 2018JD030228, ~~2019~~,
703 <https://doi.org/10.1029/2018JD030228>, [2019](#).

704 Iacono, M. J., Delamere, J. S., Mlawer, E. J., Shephard, M. W., Clough, S. A., and Collins, W. D.: Radiative forcing
705 by long-lived greenhouse gases: Calculations with the AER radiative transfer models, *J. Geophys. Res.*, 113,
706 D13103, ~~2008~~, <https://doi.org/10.1029/2008JD009944>, [2008](#).

707 Ito, A. and Feng, Y.: Role of dust alkalinity in acid mobilization of iron, *Atmos. Chem. Phys.*, 10, 9237–9250, ~~2010~~,
708 <https://doi.org/10.5194/acp-10-9237-2010>, [2010](#).

709 Ito, A. and Shi, Z.: Delivery of anthropogenic bioavailable iron from mineral dust and combustion aerosols to the
710 ocean, *Atmos. Chem. Phys.*, 16, 85–99, ~~2016~~, <https://doi.org/10.5194/acp-16-85-2016>, [2016](#).

711 Ito, A. and Kok, J. F.: Do dust emissions from sparsely vegetated regions dominate atmospheric iron supply to the
712 Southern Ocean?, *J. Geophys. Res.-Atmos.*, 122, 3987–4002, ~~2017~~, <https://doi.org/10.1002/2016JD025939>,
713 [2017](#).

714 Ito, A., Lin, G., and Penner, J. E.: Radiative forcing by lightabsorbing aerosols of pyrogenetic iron oxides, *Sci. Rep.-*
715 *UK*, 8, 7347, ~~2018~~, <https://doi.org/10.1038/s41598-018-25756-3>, [2018](#).

716 Ito, A., Myriokefalitakis, S., Kanakidou, M., Mahowald, N. M., Scanza, R. A., Hamilton, D. S., Baker, A. R., Jickells,
717 T., Sarin, M., Bikkina, S., Gao, Y., Shelley, R. U., Buck, C. S., Landing, W. M., Bowie, A. R., Perron, M.
718 M. G., Guieu, C., Meskhidze, N., Johnson, M. S., Feng, Y., Kok, J. F., Nenes, A., and Duce, R. A.: Pyrogenic

719 iron: The missing link to high iron solubility in aerosols, *Sci. Adv.*, 5, eaau7671, ~~2019~~,
720 <https://doi.org/10.1126/sciadv.aau7671>, 2019.

721 Ito, A., Perron, M. M. G., Proemse, B. C., Strzelec, M., Gault-Ringold, M., Boyd, P. W., and Bowie, A. R.: Evaluation
722 of aerosol iron solubility over Australian coastal regions based on inverse modeling: implications of bushfires
723 on bioaccessible iron concentrations in the Southern Hemisphere, *Prog. Earth Planet. Sci.*, 7, 42, ~~2020~~,
724 <https://doi.org/10.1186/s40645-020-00357-9>, 2020.

725 [Ito, A., Ye, Y., Baldo, C., and Shi, Z.: Ocean fertilization by pyrogenic aerosol iron, *npj Clim. Atmos. Sci.*, 4, 30,](#)
726 <https://doi.org/10.1038/s41612-021-00185-8>, 2021.

727 Journet, E., Balkanski, Y., and Harrison, S. P.: A new data set of soil mineralogy for dust-cycle modeling, *Atmos.*
728 *Chem. Phys.*, 14, 3801–3816, ~~2014~~, <https://doi.org/10.5194/acp-14-3801-2014>, 2014.

729 Kok, J. F.: A scaling theory for the size distribution of emitted dust aerosols suggests climate models underestimate
730 the size of the global dust cycle, *P. Natl. Acad. Sci. USA*, 108, 1016–1021, ~~2011~~,
731 <https://doi.org/10.1073/pnas.1014798108>, 2011.

732 Kok, J. F., Parteli, E. J. R., Michaels, T. I., and Karam, D. B.: The physics of wind-blown sand and dust, *Rep. Prog.*
733 *Phys.*, 75, 106901, ~~2012~~, doi:10.1088/0034-4885/75/10/106901, 2012.

734 Kok, J. F., Mahowald, N. M., Fratini, G., Gillies, J. A., Ishizuka, M., Leys, J. F., Mikami, M., Park, M.-S., Park, S.-
735 U., Van Pelt, R. S., and Zobeck, T. M.: An improved dust emission model – Part 1: Model description and
736 comparison against measurements, *Atmos. Chem. Phys.*, 14, 13023–13041, ~~2014~~,
737 <https://doi.org/10.5194/acp-14-13023-2014>, 2014.

738 Kok, J. F., Ridley, D. A., Zhou, Q., Miller, R. L., Zhao, C., Heald, C. L., Ward, D. S., Albani, S., and Haustein, K.:
739 Smaller desert dust cooling effect estimated from analysis of dust size and abundance, *Nat. Geosci.*, 10, 274–
740 278, ~~2017~~, <https://doi.org/10.1038/ngeo2912>, 2017.

741 Kok, J. F., Ward, D. S., Mahowald, N. M., and Evan, A. T.: Global and regional importance of the direct dust-climate
742 feedback, *Nat. Commun.*, 9, 241, ~~2018~~, <https://doi.org/10.1038/s41467-017-02620-y>, 2018.

743 Kok, J. F., Adebisi, A. A., Albani, S., Balkanski, Y., Checa-Garcia, R., Chin, M., Colarco, P. R., Hamilton, D. S.,
744 Huang, Y., Ito, A., Klose, M., Leung, D. M., Li, L., Mahowald, N. M., Miller, R. L., Obiso, V., Pérez García-
745 Pando, C., Rocha-Lima, A., Wan, J. S., and Whicker, C. A.: Improved representation of the global dust cycle
746 using observational constraints on dust properties and abundance, *Atmos. Chem. Phys. Discuss.*, 21, 8127–
747 [8167](#), <https://doi.org/10.5194/acp-21-8127-2021> ~~2020-1131~~, ~~in review~~, 2021.

748 Lacagnina, C., Hasekamp, O. P., Bian, H., Curci, G., Myhre, G., van Noije, T., Schulz, M., Skeie, R. B., Takemura,
749 T., and Zhang, K.: Aerosol single-scattering albedo over the global oceans: Comparing PARASOL retrievals

750 with AERONET, OMI, and AeroCom models estimates, *J. Geophys. Res.*, 120, 9814–9836, ~~2015~~,
751 <https://doi.org/10.1002/2015JD023501>, 2015.

752 Laskin, A., Iedema, M. J., Ichkovich, A., Graber, E. R., Taraniukb, I., and Yinon, R.: Direct observation of completely
753 processed calcium carbonate dust particles, *Faraday Discuss.*, 130, 453–468, ~~2005~~,
754 <https://doi.org/10.1039/B417366J>, 2005.

755 Lau, K. M., Kim, K. M., Sud, Y. C., and Walker, G. K.: A GCM study of the response of the atmospheric water cycle
756 of West Africa and the Atlantic to Saharan dust radiative forcing, *Ann. Geophys.*, 27, 4023–4037, ~~2009~~,
757 <https://doi.org/10.5194/angeo-27-4023-2009>, 2009.

758 Li, F., Vogelmann, A. M., and Ramanathan, V.: Dust aerosol radiative forcing measured from space over the Western
759 Africa, *J. Climate*, 17(13), 2558–2571, ~~2004~~, [https://doi.org/10.1175/1520-0442\(2004\)017<2558:SDARFM>2.0.CO;2](https://doi.org/10.1175/1520-0442(2004)017<2558:SDARFM>2.0.CO;2), 2004.

760

761 Li, L., and Sokolik, I. N.: The dust direct radiative impact and its sensitivity to the land surface state and key minerals
762 in the WRF-Chem-DuMo model: A case study of dust storms in Central Asia, *J. Geophys. Res.-Atmos.*, 123,
763 4564–4582, ~~2018~~, <https://doi.org/10.1029/2017JD027667>, 2018.

764 Liao, H. and Seinfeld, J.: Radiative forcing by mineral dust aerosols: sensitivity to key variables, *J. Geophys. Res.*,
765 103, 31637–31645, ~~1998~~, <https://doi.org/10.1029/1998JD200036>, 1998.

766 [Liu, X. H., Penner, J. E. and Herzog, M.: Global modeling of aerosol dynamics: Model description, evaluation, and](#)
767 [interactions between sulfate and nonsulfate aerosols, *J. Geophys. Res.*, 110, D18206,](#)
768 [doi:10.1029/2004jd005674, 2005.](#)

769 Long, L. L., Querry, M. R., Bell, R. J., and Alexander, R. W.: Optical properties of calcite and gypsum in crystalline
770 and powdered form in the infrared and far-infrared, *Infrared Phys.*, 34, 191–201, ~~1993~~,
771 [https://doi.org/10.1016/0020-0891\(93\)90008-U](https://doi.org/10.1016/0020-0891(93)90008-U), 1993.

772 Lucarini, V., Saarinen, J. J., Peiponen, K.-E., and Vartiainen, E. M.: *Kramers-Kronig relations in optical materials*
773 *research*, vol. 110, Switzerland: Springer Science & Business Media, 2005.

774 Mahowald, N., Albani, S., Kok, J. F., Engelstaeder, S., Scanza, R., Ward, D. S., and Flanner, M. G.: The size
775 distribution of desert dust aerosols and its impact on the Earth system, *Aeolian Res.*, 15, 53–71, 2014,
776 <https://doi.org/10.1016/j.aeolia.2013.09.002>, 2014.

777 Matsuki, A., Iwasaka, Y., Shi, G., Zhang, D., Trochkin, D., Yamada, M., Kim, Y.-S., Chen, B., Nagatani, T.,
778 Miyazawa, T., Nagatani, M., and Nakata, H.: Morphological and chemical modification of mineral dust:
779 Observational insight into the heterogeneous uptake of acidic gases, *Geophys. Res. Lett.*, 32, L22806, ~~2005~~,
780 <https://doi.org/10.1029/2005gl024176>, 2005.

781 Meinshausen, M., Vogel, E., Nauels, A., Lorbacher, K., Meinshausen, N., Etheridge, D. M., Fraser, P. J., Montzka, S.
782 A., Rayner, P. J., Trudinger, C. M., Krummel, P. B., Beyerle, U., Canadell, J. G., Daniel, J. S., Enting, I. G.,
783 Law, R. M., Lunder, C. R., O'Doherty, S., Prinn, R. G., Reimann, S., Rubino, M., Velders, G. J. M., Vollmer,
784 M. K., Wang, R. H. J., and Weiss, R.: Historical greenhouse gas concentrations for climate modelling
785 (CMIP6), *Geosci. Model Dev.*, 10, 2057–2116, ~~2017~~, <https://doi.org/10.5194/gmd-10-2057-2017>, ~~2017~~.

786 Meng, Z., Yang, P., Kattawar, G. W., Bi, L., Liou, K. N., and Laszlo, I.: Single-scattering properties of tri-axial
787 ellipsoidal mineral dust aerosols: a database for application to radiative transfer calculations, *J. Aerosol Sci.*,
788 41, 501–512, ~~2010~~, <https://doi.org/10.1016/j.jaerosci.2010.02.008>, ~~2010~~.

789 Miller, R. L. and Tegen, I.: Climate response to soil dust aerosols, *J. Climate*, 11, 3247–3267, ~~1998~~,
790 [https://doi.org/10.1175/1520-0442\(1998\)011<3247:CRTSDA>2.0.CO;2](https://doi.org/10.1175/1520-0442(1998)011<3247:CRTSDA>2.0.CO;2), ~~1998~~.

791 [Miller, R. L., Perlwitz, J., and Tegen, I.: Feedback upon dust emission by dust radiative forcing through the planetary](#)
792 [boundary layer, *J. Geophys. Res.*, 109, D24209, doi:10.1029/2004JD004912, 2004a.](#)

793 Miller, R. L., Tegen, I., and Perlwitz, J.: Surface radiative forcing by soil dust aerosols and the hydrologic cycle, *J.*
794 *Geophys. Res.*, 109, D04203, ~~2004~~, <https://doi.org/10.1029/2003JD004085>, ~~2004b~~.

795 [Miller, R. L., Knippertz, P., Pérez García-Pando, C., Perlwitz, J. P., and Tegen, I.: Impact of dust radiative forcing](#)
796 [upon climate. in: *Mineral Dust: A Key Player in the Earth System*, edited by: Knippertz, P. and Stuut, J.-B.](#)
797 [W., Springer, 327–357, doi:10.1007/978-94-017-8978-3_13, 2014.](#)

798 [Myriokefalitakis, S., Ito, A., Kanakidou, M., Nenes, A., Krol, M. C., Mahowald, N. M., Scanza, R. A., Hamilton, D.](#)
799 [S., Johnson, M. S., Meskhidze, N., Kok, J. F., Guieu, C., Baker, A. R., Jickells, T. D., Sarin, M. M., Bikkina,](#)
800 [S., Shelley, R., Bowie, A., Perron, M. M. G., and Duce, R. A.: Reviews and syntheses: the GESAMP](#)
801 [atmospheric iron deposition model intercomparison study, *Biogeosciences*, 15, 6659–6684,](#)
802 <https://doi.org/10.5194/bg-15-6659-2018>, 2018.

803 [Pabortsava, K., Lampitt, R. S., Benson, J., Crowe, C., McLachlan, R., Le Moigne, F. A. C., Mark Moore, C., Pebody,](#)
804 [C., Provost, P., Rees, A. P., Tilstone, G. H., and Woodward, E. M. S.: Carbon sequestration in the deep](#)
805 [Atlantic enhanced by Saharan dust. *Nat. Geosci.* 10, 189–194, 2017, https://doi.org/10.1038/ngeo2899, 2017.](#)

806 [Penner, J. E., Zhou, C., Garnier, A., and Mitchell, D. L.: Anthropogenic aerosol indirect effects in cirrus clouds. *J.*](#)
807 [Geophys. Res., 123, 11,652–11,677. <https://doi.org/10.1029/2018JD029204>, 2018.](#)

808 Penner, J.: Soot, sulfate, dust and the climate—Three ways through the fog. *Nature*, 570, 158–159, ~~2019~~,
809 <https://doi.org/10.1038/d41586-019-01791-6>, ~~2019~~.

810 [Perlwitz, J., Tegen, I., and Miller, R.: Interactive soil dust aerosol model in the GISS GCM 1. Sensitivity of the soil](#)
811 [dust cycle to radiative properties of soil dust aerosols, *J. Geophys. Res.*, 106\(D16\), 18,167–18,192,](#)
812 <https://doi.org/10.1029/2000JD900668>, 2001

813 Räsänen, P., Haapanala, P., Chung, C. E., Kahnert, M., Makkonen, R., Tonttila, J., and Nousiainen, T.: Impact of
814 dust particle nonsphericity on climate simulations, *Q. J. Roy. Meteor. Soc.*, 139, 2222–2232, ~~2013~~,
815 <https://doi.org/10.1002/qj.2084>, 2013.

816 Reichle, R. H., de Lannoy, G., Koster, R. D., Crow, W. T., Kimball, J. S., and Liu, Q.: SMAP L4 global 3-hourly 9
817 km EASE-grid surface and root zone soil moisture geophysical data, version 4. NASA National Snow and
818 Ice Data Center Distributed Active Archive Center, ~~2018~~, <https://doi.org/10.5067/kpjnn2gi1dqr>, 2018.

819 Reichle, R. H., Liu, Q., Koster, R. D., Crow, W. T., De Lannoy, G. J. M., Kimball, J. S., Ardizzone, J. V., Bosch, D.,
820 Colliander, A., Cosh, M., Kolassa, J., Mahanama, S. P., Prueger, J., Starks, P., and Walker, J. P.: Version 4
821 of the SMAP Level-4 Soil Moisture algorithm and data product. *J. Adv. Model Earth Syst.*, 11, 3106–3130,
822 ~~2019~~, <https://doi.org/10.1029/2019MS001729>, 2019.

823 Reid, E. A., Reid, J. S., Meier, M. M., Dunlap, M. R., Cliff, S. S., Broumas, A., Perry, K., and Maring, H.:
824 Characterization of African dust transported to Puerto Rico by individual particle and size segregated bulk
825 analysis, *J. Geophys. Res.*, 108, 8591, ~~2003~~, <https://doi.org/10.1029/2002JD002935>, D19, 2003.

826 Ridley, D. A., Heald, C. L., Kok, J. F., and Zhao, C.: An observationally constrained estimate of global dust aerosol
827 optical depth, *Atmos. Chem. Phys.*, 16, 15097–15117, ~~2016~~, <https://doi.org/10.5194/acp-16-15097-2016>,
828 ~~2016~~.

829 Rosenberg, P. D., Parker, D. J., Ryder, C. L., Marsham, J. H., Garcia-Carreras, L., Dorsey, J. R., Brooks, I. M., Dean,
830 A. R., Crosier, J., McQuaid, J. B., and Washington, R.: Quantifying particle size and turbulent scale
831 dependence of dust flux in the Sahara using aircraft measurements, *J. Geophys. Res.-Atmos.*, 119, 7577–
832 7598, ~~2014~~, <https://doi.org/10.1002/2013JD021255>, 2014.

833 Ryder, C. L., Highwood, E. J., Lai, T. M., Sodemann, H., and Marsham, J. H.: Impact of atmospheric transport on the
834 evolution of microphysical and optical properties of Saharan dust, *Geophys. Res. Lett.*, 40, 2433–2438, ~~2013~~,
835 <https://doi.org/10.1002/grl.50482>, 2013.

836 Ryder, C. L., Highwood, E. J., Walser, A., Seibert, P., Philipp, A., and Weinzierl, B.: Coarse and giant particles are
837 ubiquitous in Saharan dust export regions and are radiatively significant over the Sahara, *Atmos. Chem.*
838 *Phys.*, 19, 15353–15376, ~~2019~~, <https://doi.org/10.5194/acp-19-15353-2019>, 2019.

839 Sicard, M., Bertolín, S., Mallet, M., Dubuisson, P., and Comerón, A.: Estimation of mineral dust long-wave radiative
840 forcing: sensitivity study to particle properties and application to real cases in the region of Barcelona, *Atmos.*
841 *Chem. Phys.*, 14, 9213–9231, ~~2014~~, <https://doi.org/10.5194/acp-14-9213-2014>, ~~2014~~.

842 Sokolik, I. N., Toon, O. B., and Bergstrom, R. W.: Modeling the radiative characteristics of airborne mineral aerosols
843 at infrared wavelengths, *J. Geophys. Res.*, 103, 8813–8826, ~~1998~~, <https://doi.org/10.1029/98JD00049>, ~~1998~~.

844 Sokolik, I. N. and Toon, O. B.: Incorporation of mineralogical composition into models of the radiative properties of
845 mineral aerosol from UV to IR wavelengths, *J. Geophys. Res.*, 104(D8), 9423–9444, ~~1999~~,
846 <https://doi.org/10.1029/1998JD200048>, ~~1999~~.

847 Song, Q., Zhang, Z., Yu, H., Kato, S., Yang, P., Colarco, P., Remer, L. A., and Ryder, C. L.: Net radiative effects of
848 dust in the tropical North Atlantic based on integrated satellite observations and in situ measurements, *Atmos.*
849 *Chem. Phys.*, 18, 11303–11322, ~~2018~~, <https://doi.org/10.5194/acp-18-11303-2018>, ~~2018~~.

850 Stegmann, P. G. and Yang, P.: A regional, size-dependent, and causal effective medium model for Asian and Saharan
851 mineral dust refractive index spectra, *J. Aerosol Sci.*, 114, 327–341, ~~2017~~,
852 <https://doi.org/10.1016/j.jaerosci.2017.10.003>, ~~2017~~.

853 Takemura, T., Egashira, M., Matsuzawa, K., Ichijo, H., O'ishi, R., and Abe-Ouchi, A.: A simulation of the global
854 distribution and radiative forcing of soil dust aerosols at the Last Glacial Maximum, *Atmos. Chem. Phys.*, 9,
855 3061–3073, ~~2009~~, <https://doi.org/10.5194/acp-9-3061-2009>, ~~2009~~.

856 Tanaka, T. Y., Aoki, T., Takahashi, H., Shibata, K., Uchiyama, A., and Mikami, M.: Study of the sensitivity of optical
857 properties of mineral dust to the direct aerosol radiative perturbation using a global aerosol transport model,
858 *SOLA*, 3, 33–36, ~~2007~~, <https://doi.org/10.2151/sola.2007-009>, ~~2007~~.

859 Tegen, I. and Lacis, A.: Modeling of particle size distribution and its influence on the radiative properties of mineral
860 dust aerosol, *J. Geophys. Res.*, 101, 19237–19244, ~~1996~~, <https://doi.org/10.1029/95JD03610>, ~~1996~~.

861 Toth III, J. R., Rajupet, S., Squire, H., Volbers, B., Zhou, J., Xie, L., Sankaran, R. M., and Lacks, D. J.: Electrostatic
862 forces alter particle size distributions in atmospheric dust, *Atmos. Chem. Phys.*, 20, 3181–3190,
863 <https://doi.org/10.5194/acp-20-3181-2020>, 2020.

864 Tuccella, P., Curci, G., Pitari, G., Lee, S., and Jo, D. S.: Direct radiative effect of absorbing aerosols: sensitivity to
865 mixing state, brown carbon and soil dust refractive index and shape, *J. Geophys. Res.-Atmos.*, 125,
866 e2019JD030967, ~~2020~~, <https://doi.org/10.1029/2019JD030967>, ~~2020~~.

867 [van der Does, M., Korte, L. F., Munday, C. I., Brummer, G.-J. A., and Stuut, J.-B. W.: Particle size traces modern](#)
868 [Saharan dust transport and deposition across the equatorial North Atlantic, *Atmos. Chem. Phys.*, 16, 13697–](#)
869 [13710, <https://doi.org/10.5194/acp-16-13697-2016>, 2016.](#)

870 van der Does, M., Knippertz, P., Zschenderlein, P., Giles Harrison, R., and Stuut, J.-B. W.: The mysterious long-range
871 transport of giant mineral dust particles, *Sci. Adv.*, 4, eaau2768, ~~2018~~,
872 <https://doi.org/10.1126/sciadv.aau2768>, 2018.

873 Volz, F.: Infrared optical constants of aerosols at some locations, *Appl. Optics*, 22, 23, 3690–3700, ~~1983~~,
874 <https://doi.org/10.1364/AO.11.000755>, 1983.

875 Wagner, R., Ajtai, T., Kandler, K., Lieke, K., Linke, C., Müller, T., Schnaiter, M., and Vragel, M.: Complex refractive
876 indices of Saharan dust samples at visible and near UV wavelengths: a laboratory study, *Atmos. Chem. Phys.*,
877 12, 2491–2512, ~~2012~~, <https://doi.org/10.5194/acp-12-2491-2012>, 2012.

878 Wan, Z., Hook, S., and Hulley, G.: MOD11C2 MODIS/Terra Land Surface Temperature/Emissivity 8-Day L3 Global
879 0.05Deg CMG V006 [Data set]. NASA EOSDIS Land Processes DAAC, ~~2015~~,
880 <https://doi.org/10.5067/MODIS/MOD11C2.006>, 2015.

881 Wang, M. and Penner, J. E.: Aerosol indirect forcing in a global model with particle nucleation, *Atmos. Chem. Phys.*,
882 9, 239–260, <https://doi.org/10.5194/acp-9-239-2009>, 2009.

883 Wiegner, M., Gasteiger, J., Kandler, K., Weinzierl, B., Rasp, K., Esselborn, M., Freudenthaler, V., Heese, B.,
884 Toledano, C., Tesche, M., and Althausen, D.: Numerical simulations of optical properties of Saharan dust
885 aerosols with emphasis on lidar applications, *Tellus B*, 61, 180–194, ~~2009~~, <https://doi.org/10.1111/j.1600->
886 [0889.2008.00381.x](https://doi.org/10.1111/j.1600-0889.2008.00381.x), 2009.

887 Xu, L. and Penner, J. E.: Global simulations of nitrate and ammonium aerosols and their radiative effects, *Atmos.*
888 *Chem. Phys.*, 12, 9479–9504, ~~2012~~, <https://doi.org/10.5194/acp-12-9479-2012>, 2012.

889 Yang, E.-S., Gupta, P., and Christopher, S. A.: Net radiative effect of dust aerosols from satellite measurements over
890 Sahara, *Geophys. Res. Lett.*, 36, L18812, ~~2009~~, <https://doi.org/10.1029/2009GL039801>, 2009.

891 Yoshioka, M., Mahowald, N., Conley, A. J., Collins, W. D., Fillmore, D.W., Zender, C. S., and Coleman, D. B.:
892 Impact of desert dust radiative forcing on Sahel precipitation: relative importance of dust compared to sea
893 surface temperature variations, vegetation changes and greenhouse gas warming, *J. Climate*, 16, 1445–1467,
894 ~~2007~~, <https://doi.org/10.1175/JCLI4056.1>, 2007.

895 Zhang, D., and Iwasaka, Y.: Size change of Asian dust particles caused by sea salt interaction: Measurements in
896 southwestern Japan, *Geophys. Res. Lett.*, 31, L15102, ~~2004~~, <https://doi.org/10.1029/2004GL020087>, 2004.

897 Zhang, J. and Christopher, S. A.: Longwave radiative forcing of Saharan dust aerosols estimated from MODIS, MISR,
898 and CERES observations on Terra, *Geophys. Res., Lett.*, 30(23), 2188, ~~2003~~,
899 <https://doi.org/10.1029/2003GL018479>, 2003.

900 Zhao, C., Chen, S., Leung, L. R., Qian, Y., Kok, J. F., Zaveri, R. A., and Huang, J.: Uncertainty in modeling dust mass
901 balance and radiative forcing from size parameterization, *Atmos. Chem. Phys.*, 13, 10733–10753, ~~2013~~,
902 <https://doi.org/10.5194/acp-13-10733-2013>, 2013.

903 Zhou, Y., Levy, R. C., Remer, L. A., Mattoo, S., and Espinosa, W. R.: Dust aerosol retrieval over the oceans with the
904 MODIS/VIIRS dark target algorithm: 2. Nonspherical dust model, *Earth Space Sci.*, 7, e2020EA001222,
905 ~~2020~~, <https://doi.org/10.1029/2020EA001222>, 2020.

906 **Figure captions**

907 Figure 1. Imaginary part of the refractive index at [a wavelength of 0.52 \$\mu\$ m SW](#) and [9.7 \$\mu\$ m LW](#) for the nine main
908 source regions and the global mean for others. The refractive index obtained from 19 samples was aggregated
909 into 9 main source regions and the arithmetic mean was calculated for each source region (Di Biagio et al.,
910 2017, 2019). The coordinates of the nine source regions were: ([S1](#)) western North Africa (20°W – 7.5°E;
911 18°N – 37.5°N), ([S2](#)) eastern North Africa (7.5°E – 35°E; 18°N – 37.5°N), ([S3](#)) the Sahel (20°W – 35°E;
912 0°N – 18°N), ([S4](#)) Middle East / Central Asia (30°E – 70°E for 0°N – 35°N, and 30°E – 75°E for 35°N –
913 50°N), ([S5](#)) East Asia (70°E – 120°E; 35°N – 50°N), ([S6](#)) North America (130°W – 80°W; 20°N – 45°N),
914 ([S7](#)) Australia (110°E – 160°E; 10°S – 40°S), ([S8](#)) South America (80°W – 20°W; 0°S – 60°S), and ([S9](#))
915 Southern Africa (0°E – 40°E; 0°S – 40°S).

916 ~~Figure 2. ——— Model simulated dust loads at fine (smaller than 2.5 μ m of diameter) and coarse size ranges (larger
917 than 2.5 μ m of diameter) before and after adjusting the size-resolved dust load with DustCOMM. Results
918 were shown for (a) fine dust from DustCOMM, (b) fine dust from [IMPACT Sphere Mineral V83 \(E1\) default](#),
919 (c) fine dust from [DustCOMM-Asphere-DB19-V83 \(E2\) improved](#), (d) coarse dust from DustCOMM, (e)
920 coarse dust from [E1, default](#) and (f) coarse dust from [E2 improved](#) simulations. The parentheses represented
921 the global dust burden (T_g). The values of dust load at each bin were listed in Table 3.~~

922 Figure [32](#). The model better reproduced semi-observationally-based data of DAOD₅₅₀ ~~in boreal summer (June,~~
923 ~~July, and August)~~ after [adjusting the size-resolved dust load with DustCOMM and](#) considering the dust
924 asphericity. (a) semi-observationally-based estimates of the DAOD₅₅₀ were averaged over 2004–2008
925 (Ridley et al., 2016; Adebisi et al., 2020). The [annually averaged](#) model results were shown for (b) ~~default~~
926 [DustCOMM-Asphere-DB19-V83 \(E2\)](#), and (c) ~~the differences between improved IMPACT-Sphere-Mineral-~~
927 ~~V83 (E1) and E2, and (d) fine global~~ simulations. [\(d\) Comparison of seasonally averaged DAOD₅₅₀ for semi-](#)
928 [observationally-based \(SOB\) data, E1, E2, IMPACT-Asphere-DB19-DB17 \(E3\), and DustCOMM-Sphere-](#)
929 [DB19-DB17 \(E5\).](#) The square symbol represents the mean. The solid line within the box mark shows the
930 [median. The boundaries of the box mark the 25th and 75th percentiles. The whiskers above and below the](#)
931 [box indicate the 1.5 \$\times\$ interquartile range, and the points indicate the outside of the range.](#) (e) [Taylor diagram](#)
932 [summarizing the statistics of the comparison against the seasonally averaged regional DAOD₅₅₀ for the](#)
933 [different experiments. The horizontal axis shows the standard deviation of the data set or model prediction,](#)
934 [the curved axis shows the correlation, and the green dashed lines denote the root-mean-squared errors](#)
935 [between the semi-observationally-based data and the model predictions. As such, the distance between the](#)
936 [semi-observationally-based data and the model predictions is a measure of the model's ability to reproduce](#)

937 the spatiotemporal variability in the semi-observationally-based data. The coordinates of the fifteen regions
938 were: (A1) Mid-Atlantic (4°–40°N, 50°–20°W), (A2) African West Coast (10°–34°N, 20°–5°W), (A3)
939 Northern Africa (26°–40°N, 5°W–30°E), (A4) Mali/Niger (10°–26°N, 5°W–10°E), (A5) Bodele/Sudan
940 (10°–26°N, 10°–40°E), (A6) Northern Middle East (26°–40°N, 30°–50°E), (A7) Southern Middle East (0°–
941 26°N, 40°–67.5°E), (A8) Kyzyl Kum (26°–50°N, 50°–67.5°E), (A9) Thar (20°–50°N, 67.5°–75°E), (A10)
942 Taklamakan (30°–50°N, 75°–92.5°E), (A11) Gobi (36°–50°N, 92.5°–115°E), (A12) North America (20°–
943 45°N, 80°–130°W), (A13) South America (0°–55°S, 80°–55°W), (A14) Southern Africa (10°–35°S, 10°–
944 40°E), and (A15) Australia (10°–40°S, 110°–160°E). The values of DAOD₅₅₀ at the 15 regions (marked in
945 Fig. 3a) in summer were listed in Table S1. ~~The scatter plot was shown in Fig. S1. The summer season was~~
946 ~~shown because most semi-observation based data on dust radiative effects were available.~~ The comparison
947 for other seasons was presented in Table S2.

948 Figure 3. Model-simulated dust loads at fine (smaller than 2.5 μm of diameter) and coarse size ranges (larger
949 than 2.5 μm of diameter) before and after adjusting the size-resolved dust load with DustCOMM. Results
950 were shown for (a) fine dust from DustCOMM, (b) fine dust from IMPACT-Sphere-Mineral-V83 (E1), (c)
951 fine dust from DustCOMM-Asphere-DB19-V83 (E2), (d) coarse dust from DustCOMM, (e) coarse dust from
952 E1, and (f) coarse dust from E2 simulations. The parentheses represented the global dust burden (T_g). The
953 values of dust load at each bin were listed in Table 3.

954 Figure 4. ~~Summertime~~ ~~D~~ust clear-sky SW radiative effect efficiency ($W \cdot m^{-2} \cdot DAOD^{-1}$). Semi-
955 observationally-based data at (a) the surface and (b) TOA were based on satellite observations (Yang et al.
956 2009; Li et al., 2004; Song et al., 2018; Christopher and Jones, 2007). The model results were shown for (c)
957 and (d) IMPACT-Sphere-Mineral-V83 (E1) ~~default~~, and (e) and (f) DustCOMM-Asphere-DB19-V83
958 (E2) ~~improved~~ simulations at the surface and TOA, respectively. (g) Comparison of seasonally averaged SW
959 radiative effect efficiency for semi-observationally-based (SOB) data and the different experiments. The
960 square symbol represents the mean. The solid line within the box mark shows the median. The boundaries of
961 the box mark the 25th and 75th percentiles. The whiskers above and below the box indicate the 1.5 ×
962 interquartile range, and the points indicate the outside of the range. (h) Taylor diagram summarizing the
963 statistics of the comparison against the seasonally averaged regional SW radiative effect efficiency for the
964 different experiments. The horizontal axis shows the standard deviation of the data set or model prediction,
965 the curved axis shows the correlation, and the green dashed lines denote the root-mean-squared errors
966 between the semi-observationally-based data and the model predictions. As such, the distance between the
967 semi-observationally-based data and the model predictions is a measure of the model's ability to reproduce

968 the spatiotemporal variability in the semi-observationally-based data. The regionally averaged values were
969 listed in Tables S3 and S4 at the surface and TOA, respectively. ~~The scatter plot was shown in Fig. S2. The~~
970 ~~results from other sensitivity simulations were also shown in Fig. S3.~~

971 Figure 5. ~~Summertime~~ dDust clear-sky LW radiative effect efficiency ($W \cdot m^{-2} DAOD_{550}^{-1}$). Semi-
972 observationally-based estimates at (a) surface and (b) TOA were based on satellite observations (Song et al.,
973 2018; Christopher and Jones, 2007; Zhang and Christopher, 2003; Brindley and Russell, 2009; Yang et al.,
974 2009). The model results were shown for (c) and (d) IMPACT-Sphere-Mineral-V83 (E1)default, and (e) and
975 (f) DustCOMM-Asphere-DB19-V83 (E2)improved simulations at the surface and TOA, respectively. (g)
976 Comparison of seasonally averaged LW radiative effect efficiency for semi-observationally-based (SOB)
977 data and the different experiments. The square symbol represents the mean. The solid line within the box
978 mark shows the median. The boundaries of the box mark the 25th and 75th percentiles. The whiskers above
979 and below the box indicate the $1.5 \times$ interquartile range, and the points indicate the outside of the range. (h)
980 Taylor diagram summarizing the statistics of the comparison against the seasonally averaged regional SW
981 radiative effect efficiency for the different experiments. The horizontal axis shows the standard deviation of
982 the data set or model prediction, the curved axis shows the correlation, and the green dashed lines denote the
983 root-mean-squared errors between the semi-observationally-based data and the model predictions. As such,
984 the distance between the semi-observationally-based data and the model predictions is a measure of the
985 model's ability to reproduce the spatiotemporal variability in the semi-observationally-based data. The
986 regionally averaged values were listed in Tables S5 and S6 at the surface and TOA, respectively. ~~The scatter~~
987 ~~plot was shown in Fig. S4. The results from other sensitivity simulations were also shown in Fig. S5.~~

988 Figure 6. Dust SW radiative effect ($W \cdot m^{-2}$) and radiative heating of the atmosphere (i.e., the subtraction of
989 radiative effects from TOA to the surface in unit of $W \cdot m^{-2}$). The model results were shown for the simulations
990 for (a) IMPACT-Sphere-Mineral-V83 (E1)default at the surface, (b) DustCOMM-Asphere-DB19-V83
991 (E2)improved at the surface, (c) E1default in atmospheric column, (d) E2improved in atmospheric column,
992 (e) E1default at TOA, and (f) E2improved simulations at TOA. The numbers in parentheses represented the
993 global mean.

994 Figure 7. Dust LW radiative effect ($W \cdot m^{-2}$) and radiative heating of the atmosphere (i.e., the subtraction of
995 radiative effects from TOA to the surface in unit of $W \cdot m^{-2}$). The model results were shown for the simulations
996 for (a) IMPACT-Sphere-Mineral-V83 (E1)default at the surface, (b) DustCOMM-Asphere-DB19-V83
997 (E2)improved at the surface, (c) E1default in atmospheric column, (d) E2improved in atmospheric column,

998 (e) [E1default](#) at TOA, and (f) [E2improved](#) simulations at TOA. The numbers in parentheses represented the
999 global mean.

1000 Figure 8. Dust radiative effect ($\text{W}\cdot\text{m}^{-2}$) and radiative heating of the atmosphere (i.e., the subtraction of
1001 radiative effects from TOA to the surface in unit of $\text{W}\cdot\text{m}^{-2}$). The model results were shown for the simulations
1002 for (a) [IMPACT-Sphere-Mineral-V83 \(E1\)default](#) at the surface, (b) [DustCOMM-Asphere-DB19-V83](#)
1003 [\(E2\)improved](#) at the surface, (c) [E1default](#) in atmospheric column, (d) [E2improved](#) in atmospheric column,
1004 (e) [E1default](#) at TOA, and (f) [E2improved](#) simulations at TOA. The numbers in parentheses represented the
1005 global mean.

1006 Figure 9. Radiative effect ($\text{W}\cdot\text{m}^{-2}$) of mineral dust due to different studies at the surface and TOA for (a) total
1007 dust SW, (b) total dust LW, and (c) total dust NET. The annually averaged values were listed in Table 5.

1008 [Figure 10.](#) Radiative effect ($\text{W}\cdot\text{m}^{-2}$) of mineral dust due to various aerosol absorptivity at the surface and TOA
1009 for (a) total dust SW, (b) total dust LW, and (c) total dust NET. The annually averaged values were listed in
1010 Table 5. The dashed line represented a 1 : 1 correspondence and corresponded to no change in radiative
1011 heating within the atmosphere.

Table 1. Summary of ~~seven~~ [simulations-experiments](#) compared in this study.

Number Experiment	Simulation Experiment	Size-resolved dust	Sphericity	SW refractive index	LW refractive index
Experiment-1	IMPACT-Sphere-Mineral-V83DB17Default	IMPACT	Spherical	Mineralogical map ^d	Volz (1983)Di Biagio et al. (2017)
Experiment-2 ^a	DustCOMM-Asphere-DB19-V83Improved	DustCOMM ^b	Aspherical ^c	Di Biagio et al. (2019)	Volz (1983)
Experiment-3	IMPACTFine-Asphere-DB19-DB17global	IMPACT	Aspherical ^c	Di Biagio et al. (2019)	Di Biagio et al. (2017)
Experiment-4	DustCOMMCoarse-Asphere-DB19-DB17global	DustCOMM ^b	Aspherical ^c	Di Biagio et al. (2019)	Di Biagio et al. (2017)
E5	DustCOMM-Sphere-DB19-DB17	DustCOMM^b	Spherical	Di Biagio et al. (2019)	Di Biagio et al. (2017)
Experiment-5	DustCOMMCoarse-Asphere-Rregion	DustCOMM^b	Aspherical^e	Regional mean^e	Regional mean^e
Experiment-6	DustCOMMCoarse-Asphere-Mineral-V83	DustCOMM ^b	Aspherical ^c	Mineralogical map ^d	Volz (1983)
Experiment-7	DustCOMMCoarse-Asphere-Less-Moreabsorption	DustCOMM ^b	Aspherical ^c	Less SW ^{fe}	More LW ^g
E8	DustCOMM-Asphere-Less-Less	DustCOMM^b	Aspherical^c	Less SW^e	Less LW^h
E9	DustCOMM-Asphere-More-More	DustCOMM^b	Aspherical^c	More SW^f	More LW^g
E10	DustCOMM-Asphere-More-Less	DustCOMM^b	Aspherical^c	More SW^f	Less LW^h

^aCombination of DustCOMM-Asphere-DB19-DB17 (~~Experiment-4~~) for SW and DustCOMM-Asphere-Mineral-V83 (~~Experiment-7~~) for LW.

^bSize-resolved dust concentration was adjusted with semi-observationally-based estimate (Adebisi & Kok, 2020).

^cDust asphericity was considered in calculating the [optical properties refractive index](#), which further assumed internal mixing of minerals (Huang et al., 2020b) using a volume-weighted mixture for each size bin.

^dMineralogical composition of dust aerosol for each size was prescribed at emission by mineralogical map (Journet et al., 2014; Ito and Shi 2016). The more absorptive SW refractive indices (Bedidi and Cervelle, 1993; Stegmann & Yang, 2017; Long et al., 1993) were used for mineral dust, compared to the less absorptive global mean data set (Di Biagio et al., 2019).

^e[Regional mean of refractive index was calculated for the nine main source regions \(Fig. 1\). The global mean was used for other areas.](#)

^fLess absorptive SW refractive indices were calculated by varying the values of the imaginary parts of the refractive index within the range of values from Di Biagio et al. (2019) (10% percentile).

^fMore absorptive SW refractive indices were calculated by varying the values of the imaginary parts of the refractive index within the range of values from Di Biagio et al. (2019) (90% percentile).

^gMore absorptive LW refractive indices were calculated by varying the values of the imaginary parts of the refractive index within the range of values from Di Biagio et al. (2017) (90% percentile).

^hLess absorptive LW refractive indices were calculated by varying the values of the imaginary parts of the refractive index within the range of values from Di Biagio et al. (2017) (10% percentile).

Table 2. Summary of radiative effects estimated in this study.

SW radiative effect	LW radiative effect	Difference
Less absorptive SW, coarser particle size, & aspherical shape	More absorptive LW, coarser particle size, & aspherical shape	Experiment 2 – Experiment 1
Less absorptive SW & aspherical shape	Less absorptive LW & aspherical shape	Experiment 3 – Experiment 1
Size-resolved dust abundance	Size-resolved dust abundance	Experiment 3 – Experiment 4
Aspherical shape	Aspherical shape	E5 – E4
Regional variability in refractive index	Regional variability in refractive index	Experiment 5 – Experiment 4
Mineralogical variability in refractive index (more absorptive SW)	Mineralogical variability in refractive index (more absorptive LW)	Experiment 6 – Experiment 4
Less absorptive SW (10% percentile)	More absorptive LW (90% percentile)	Experiment 7 – Experiment 4
Less absorptive SW (10% percentile)	Less absorptive LW (10% percentile)	E8 – E4
More absorptive SW (90% percentile)	More absorptive LW (90% percentile)	E9 – E4
More absorptive SW (90% percentile)	Less absorptive LW (10% percentile)	E10 – E4

Table 3. Annually averages of dust load (Tg), mass extinction efficiency ($\text{m}^2 \cdot \text{g}^{-1}$), and DAOD₅₅₀ at each bin on a global scale. The size-resolved dust concentration and shape in [IMPACT-Sphere-Mineral-V83 \(E1\)the default](#) simulation was adjusted to DustCOMM in [DustCOMM-Asphere-DB19-V83 \(E2\)the improved](#) simulation. At the same time, we maintained the consideration of asphericity on the gravitational velocity and kept the dust concentrations unaltered between [IMPACT-Sphere-Mineral-V83 \(E1\)the default](#) and [IMPACT-Asphere-DB19-DB17fine global](#) simulations [\(E3\)](#).

Dust size bin	Dust load			Mass extinction efficiency				DAOD ₅₅₀			
	E1Default	E2Improved	DustCOMM	E1Default	E2Improved	E3Fine-global	DustCOMM	E1Default	E2Improved	E3Fine-global	DustCOMM
Bin 1 ^a	1.2	0.8	1.2 ± 0.7	2.11	3.41	3.33	3.06	0.0050	0.0055	0.0078	0.0070
Bin 2 (1.26–2.5 μm)	4.7	2.6	3.5 ± 2.1	0.73	1.25	1.21	1.22	0.0067	0.0064	0.0111	0.0084
Bin 3 (2.5–5 μm)	8.2	6.2	6.8 ± 3.8	0.37	0.59	0.57	0.57	0.0060	0.0071	0.0092	0.0077
Bin 4 (5–20 μm)	10.9	22.2	16.8 ± 9.0	0.23	0.24	0.29	0.19	0.0050	0.0104	0.0063	0.0063
Sum of 4 bins	25.0	31.8	28.4 ± 15.5	0.46	0.47	0.70	0.53	0.0227	0.0295	0.0345	0.0294

^aBin 1 in [IMPACT-Sphere-Mineral-V83 \(E1\)the default model](#) is 0.1–1.26 μm, whereas bin1 in [DustCOMM-Asphere-DB19-V83 \(E2\)the improved model](#) and DustCOMM is 0.2–1.26 μm.

Table 4. Semi-observationally-based data set of clear-sky dust radiative effect efficiency at the surface and TOA.

Number	Region name	Season	Region coordinates	Aerosol type selection	AOD data
R1 ^a	Sahara Desert	Summer	15°–30°N, 10°W–30°E	No selection	OMI-MISR
R2 ^b	Tropical Atlantic	Summer	15°–25°N, 45°–15°W	MODIS effective radius peaks 0.8–0.9 μm	MODIS
R3 ^c	Tropical Atlantic	Summer	10°–30°N, 45°–20°W	CALIOP dust and polluted dust	CERES-CALIPSO-CloudSat-MODIS
R4 ^d	Atlantic Ocean	Summer	0°–30°N, 60°–10°W	Dust detection based on DAOD ₅₅₀ and fraction	MODIS
R5 ^{e,f}	North Africa	Summer	15°–35°N, 18°W–40°E	No selection	MISR ^e or SEVIRI ^f
R6 ^{e,f}	West Africa	Summer	16°–28°N, 16°–4°W	No selection	MISR ^e or SEVIRI ^f
R7 ^{e,f}	Niger-Chad	Summer	15°–20°N, 15°–22°E	No selection	MISR ^e or SEVIRI ^f
R8 ^{e,f}	Sudan	Summer	15°–22°N, 22°–36°E	No selection	MISR ^e or SEVIRI ^f
R9 ^{e,f}	Egypt-Israel	Summer	23°–32°N, 23°–35°E	No selection	MISR ^e or SEVIRI ^f
R10 ^{e,f}	North Libya	Summer	27°–33°N, 15°–25°E	No selection	MISR ^e or SEVIRI ^f
R11 ^{e,f}	South Libya	Summer	23°–27°N, 15°–25°E	No selection	MISR ^e or SEVIRI ^f
R12 ^g	Mediterranean	Summer	35.5°N, 12.6°E	Dust detection based on optical property	Ground-based measurements
R13 ^h	Cape Verde	Summer	16.7°N, 22.9°E	Dust detection based on brightness temperature	Ground-based measurements
R14 ⁱ	China	Spring	39°N, 101°E	Dust detection based on brightness temperature	Ground-based measurements

^aYang et al. (2009). ^bLi et al. (2004). ^cSong et al. (2018). ^dChristopher and Jones (2007). ^eZhang and Christopher (2003). ^fBrindley and Russell (2009). ^gDi Biagio et al. (2010). ^hHansell et al. (2010). ⁱHansell et al. (2012).

Table 5. Annually averages of short-wave (SW) ($W \cdot m^{-2}$), long-wave (LW) ($W \cdot m^{-2}$), and net radiative effect (NET) ($W \cdot m^{-2}$) at the surface, TOA, and atmospheric radiative heating on a global scale.

Number	Data	Total dust SW		Total dust LW		Total dust NET	
		TOA (surface) ^a	Atmosphere	TOA (surface) ^a	Atmosphere	TOA (surface) ^a	Atmosphere
Experiment 1	IMPACT-Sphere-Mineral-V83DB17Default	-0.18 (-1.326)	1.07	+0.09-18 (0.3766)	-0.2948	-0.009 (-0.8860)	0.579
Experiment 2	DustCOMM-Asphere-DB19-V83Improved	-0.32 (-1.23)^b	0.91^b	+0.23 (1.00)^b	-0.77^b	-0.08 (-0.23)^b	0.15^b
Experiment 3	IMPACTFine-Asphere-DB19-DB17global	-0.49 (-1.35)	0.86	+0.12 (0.50)	-0.38	-0.37 (-0.84)	0.48
Experiment 4	DustCOMMCoarse-Asphere-DB19-DB17global	-0.32 (-1.23)^b	0.91^b	+0.12± (0.58)	-0.46	-0.20 (-0.65)	0.45
E5	DustCOMM-Sphere-DB19-DV17	-0.28 (-0.90)	0.62	+0.08 (0.43)	-0.34	-0.20 (-0.47)	0.28
Experiment 5	DustCOMM-AsphereCoarse-Region	-0.33 (-1.20)	0.87	+0.11 (-0.53)	-0.43	-0.23 (-0.67)	0.44
Experiment 6	DustCOMM-AsphereCoarse-Mineral-V83	+0.02 (-1.61)	1.63	+0.23 (1.00)^b	-0.77^b	+0.25 (-0.62)	0.87
Experiment 7	DustCOMM-AsphereCoarse-Less-Moreabsorption	-0.54 (-1.098)	0.43	+0.16 (0.76)	-0.60	-0.38 (-0.22)	-0.16
E8	DustCOMM-Asphere-Less-Less	-0.54 (-1.098)	0.43	+0.06 (0.35)	-0.29	-0.48 (-0.36)	0.15
E9	DustCOMM-Asphere-More-More	-0.08 (-1.151)	1.43	+0.16 (0.76)	-0.60	+0.09 (-0.75)	0.84
E10	DustCOMM-Asphere-More-Less	-0.08 (-1.151)	1.43	+0.06 (0.35)	-0.29	-0.01 (-1.16)	1.15
	DustCOMM (Adebisi & Kok, 2020)	-0.59 to 0.17^c 0.43 ± 0.21		+0.25 to 0.41^c + 0.32 ± 0.08		-0.27 to 0.14^c - 0.11 ± 0.10	

M1	Miller et al. (2004b)	<u>-0.33 (-1.82)</u>	<u>1.49</u>	<u>+0.15 (0.18)</u>	<u>-0.03</u>	<u>-0.18 (-1.64)</u>	<u>1.46</u>
M2	Tanaka et al. (2007)	<u>-0.38 (-1.22)</u>	<u>0.84</u>	<u>+0.16 (0.57)</u>	<u>-0.41</u>	<u>-0.22 (-0.65)</u>	<u>0.43</u>
M3	Yoshioka et al. (2007)	<u>-0.92 (-1.59)</u>	<u>0.67</u>	<u>+0.31 (1.13)</u>	<u>-0.81</u>	<u>-0.60 (-0.46)</u>	<u>-0.14</u>
M4	Takemura et al. (2009)	<u>-0.10 (-0.38)</u>	<u>0.28</u>	<u>+0.09 (0.18)</u>	<u>-0.09</u>	<u>-0.01 (-0.20)</u>	<u>0.19</u>
M5	Albani et al. (2014)	<u>-0.38 (-1.20)</u>	<u>0.81</u>	<u>+0.15 (0.64)</u>	<u>-0.49</u>	<u>-0.23 (-0.56)</u>	<u>0.33</u>
M6	Colarco et al. (2014)	<u>-0.32 (-1.25)</u>	<u>0.93</u>	<u>+0.05 (0.30)</u>	<u>-0.25</u>	<u>-0.27 (-0.95)</u>	<u>0.68</u>
M7	Di Biagio et al. (2020)	<u>-0.29 (-1.17)^d</u>	<u>0.88^d</u>	<u>+0.23 (0.48)^d</u>	<u>-0.26^d</u>	<u>-0.06 (-0.69)^d</u>	<u>0.63^d</u>

^aThe parentheses represent the RE at the surface. ^bThe bold represents the combination of ~~DB19coarse-global~~ for SW and ~~V83coarse-mineral~~ for LW (i.e., [DustCOMM-Asphere-DB19-V83improved-simulation](#)). ^c98% confidential interval of DustCOMM data set is listed. ^dFor a comparison with our estimates, sum of single mode simulations from Di Biagio et al. (2019) is listed.

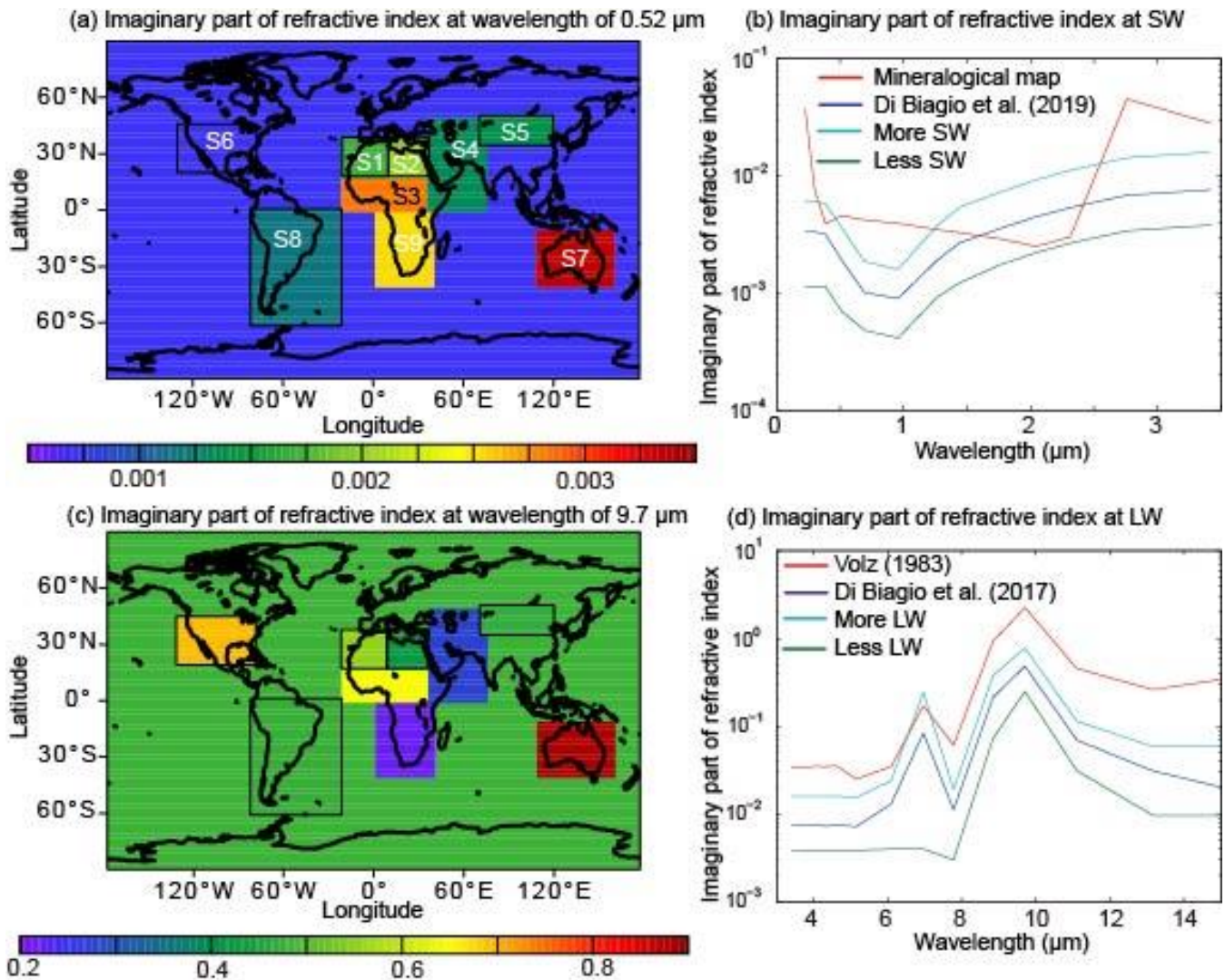


Figure 1. Imaginary part of the refractive index at a wavelength of 0.52 μm SW and 9.7 μm LW for the nine main source regions and the global mean for others. The refractive index obtained from 19 samples was aggregated into 9 main source regions and the arithmetic mean was calculated for each source region (Di Biagio et al., 2017, 2019). The coordinates of the nine source regions were: (S1) western North Africa (20°W – 7.5°E; 18°N – 37.5°N), (S2) eastern North Africa (7.5°E – 35°E; 18°N – 37.5°N), (S3) the Sahel (20°W – 35°E; 0°N – 18°N), (S4) Middle East / Central Asia (30°E – 70°E for 0°N – 35°N, and 30°E – 75°E for 35°N – 50°N), (S5) East Asia (70°E – 120°E; 35°N – 50°N), (S6) North America (130°W – 80°W; 20°N – 45°N), (S7) Australia (110°E – 160°E; 10°S – 40°S), (S8) South America (80°W – 20°W; 0°S – 60°S), and (S9) Southern Africa (0°E – 40°E; 0°S – 40°S).

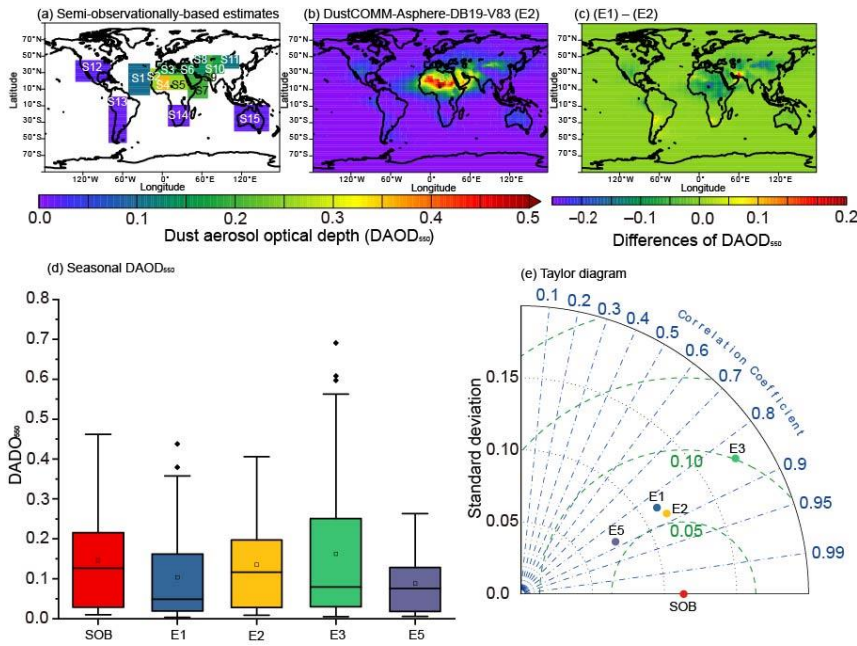
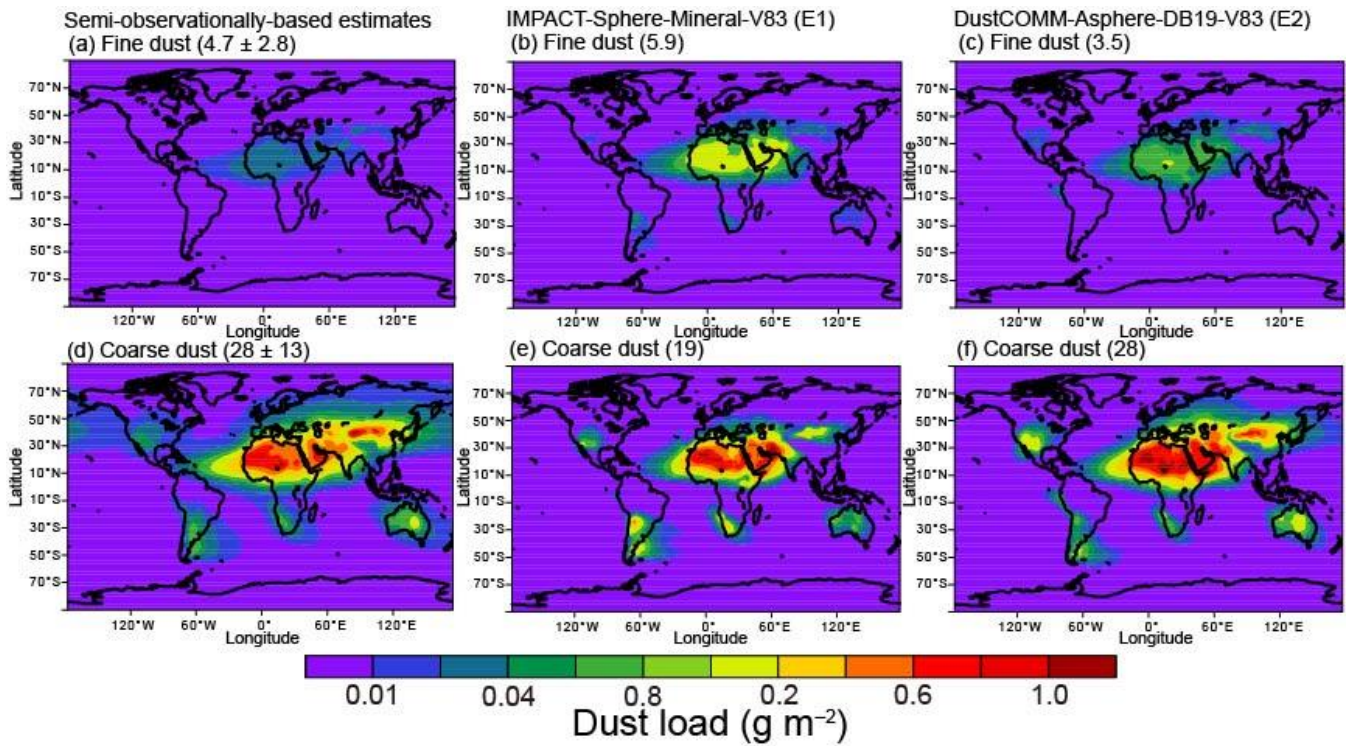


Figure 32. The model better reproduced semi-observationally-based data of DAOD₅₅₀ in boreal summer (June, July, and August) after adjusting the size-resolved dust load with DustCOMM and considering the dust asphericity. (a) semi-observationally-based estimates of the DAOD₅₅₀ were averaged over 2004–2008 (Ridley et al., 2016; Adebisi et al., 2020). The annually averaged model results were shown for (b) default DustCOMM-Asphere-DB19-V83 (E2), and (c) the differences between improved IMPACT-Sphere-Mineral-V83 (E1) and E2, and (d) fine global simulations. (d) Comparison of seasonally averaged DAOD₅₅₀ for semi-observationally-based (SOB) data, E1, E2, IMPACT-Asphere-DB19-DB17 (E3), and DustCOMM-Sphere-DB19-DB17 (E5). The square symbol represents the mean. The solid line within the box mark shows the median. The boundaries of the box mark the 25th and 75th percentiles. The whiskers above and below the box indicate the 1.5 × interquartile range, and the points indicate the outside of the range. (e) Taylor diagram summarizing the statistics of the comparison against the seasonally averaged regional DAOD₅₅₀ for the different experiments. The horizontal axis shows the standard deviation of the data set or model prediction, the curved axis shows the correlation, and the green dashed lines denote the root-mean-squared errors between the semi-observationally-based data and the model predictions. As such, the distance between the semi-observationally-based data and the model predictions is a measure of the model’s ability to reproduce the spatiotemporal variability in the semi-observationally-based data. The coordinates of the fifteen regions were: (A1) Mid-Atlantic (4°–40°N, 50°–20°W), (A2) African West Coast (10°–34°N, 20°–5°W), (A3) Northern Africa (26°–40°N, 5°W–30°E), (A4) Mali/Niger (10°–26°N, 5°W–10°E), (A5) Bodele/Sudan (10°–26°N, 10°–40°E), (A6) Northern Middle East (26°–40°N, 30°–50°E), (A7) Southern Middle East (0°–26°N, 40°–67.5°E), (A8) Kyzyl Kum (26°–50°N, 50°–67.5°E), (A9) Thar (20°–50°N, 67.5°–75°E), (A10) Taklamakan (30°–50°N, 75°–92.5°E), (A11) Gobi (36°–50°N, 92.5°–115°E), (A12) North America (20°–45°N, 80°–130°W), (A13) South America (0°–55°S, 80°–55°W), (A14) Southern Africa (10°–35°S, 10°–40°E), and (A15) Australia (10°–40°S, 110°–160°E). The values of DAOD₅₅₀ at the 15 regions (marked in Fig. 32a) in summer were

listed in Table S1. ~~The scatter plot was shown in Fig. S1. The summer season was shown because most semi-observation-based data on dust radiative effects were available.~~ The comparison for other seasons was presented in Table S2.



35 **Figure 23.** Model-simulated dust loads at fine (smaller than 2.5 μm of diameter) and coarse size ranges (larger than 2.5 μm of diameter) before and after adjusting the size-resolved dust load with DustCOMM. Results were shown for (a) fine dust from DustCOMM, (b) fine dust from [IMPACT-Sphere-Mineral-V83 \(E1\) default](#), (c) fine dust from [DustCOMM-Asphere-DB19-V83 \(E2\) improved](#), (d) coarse dust from DustCOMM, (e) coarse dust from [E1 default](#) and (f) coarse dust from [E2 improved](#) simulations. The parentheses represented the global dust burden (Tg). The values of dust load at each bin were listed in Table

40 3.

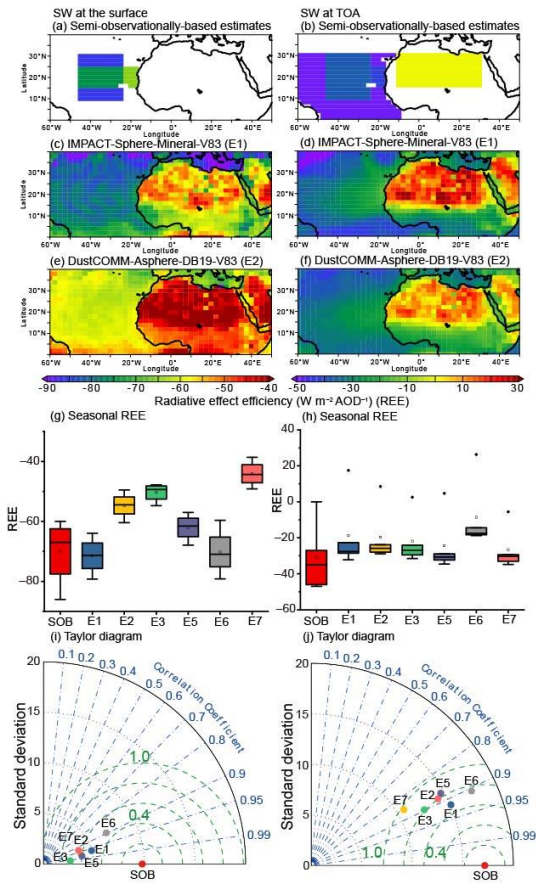


Figure 4. Summertime-Dust clear-sky SW radiative effect efficiency ($W \cdot m^{-2} DAOD^{-1}$). Semi-observationally-based data at (a) the surface and (b) TOA were based on satellite observations (Yang et al. 2009; Li et al., 2004; Song et al., 2018; Christopher and Jones, 2007). The model results were shown for (c) and (d) IMPACT-Sphere-Mineral-V83 (E1) default, and (e) and (f) DustCOMM-Asphere-DB19-V83 (E2) improved simulations at the surface and TOA, respectively. (g) Comparison of seasonally averaged SW radiative effect efficiency for semi-observationally-based (SOB) data and the different experiments. The square symbol represents the mean. The solid line within the box mark shows the median. The boundaries of the box mark the 25th and 75th percentiles. The whiskers above and below the box indicate the $1.5 \times$ interquartile range, and the points indicate the outside of the range. (h) Taylor diagram summarizing the statistics of the comparison against the seasonally averaged regional SW radiative effect efficiency for the different experiments. The horizontal axis shows the standard deviation of the data set or model prediction, the curved axis shows the correlation, and the green dashed lines denote the root-mean-squared errors between the semi-observationally-based data and the model predictions. As such, the distance between the semi-observationally-based data and the model predictions is a measure of the model's ability to reproduce the spatiotemporal variability in the semi-observationally-based data. The regionally averaged values were listed in Tables S3 and S4 at the surface and TOA, respectively. The scatter plot was shown in Fig. S2. The results from other sensitivity simulations were also shown

in Fig. S3.

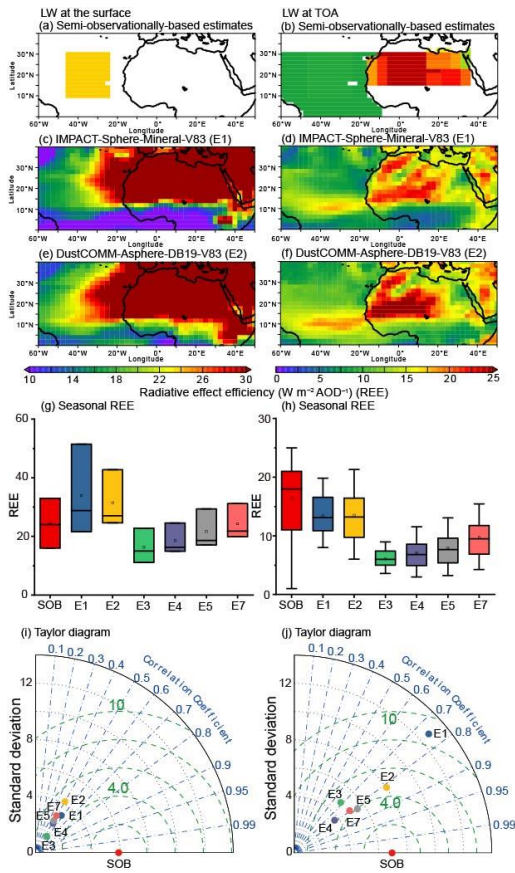
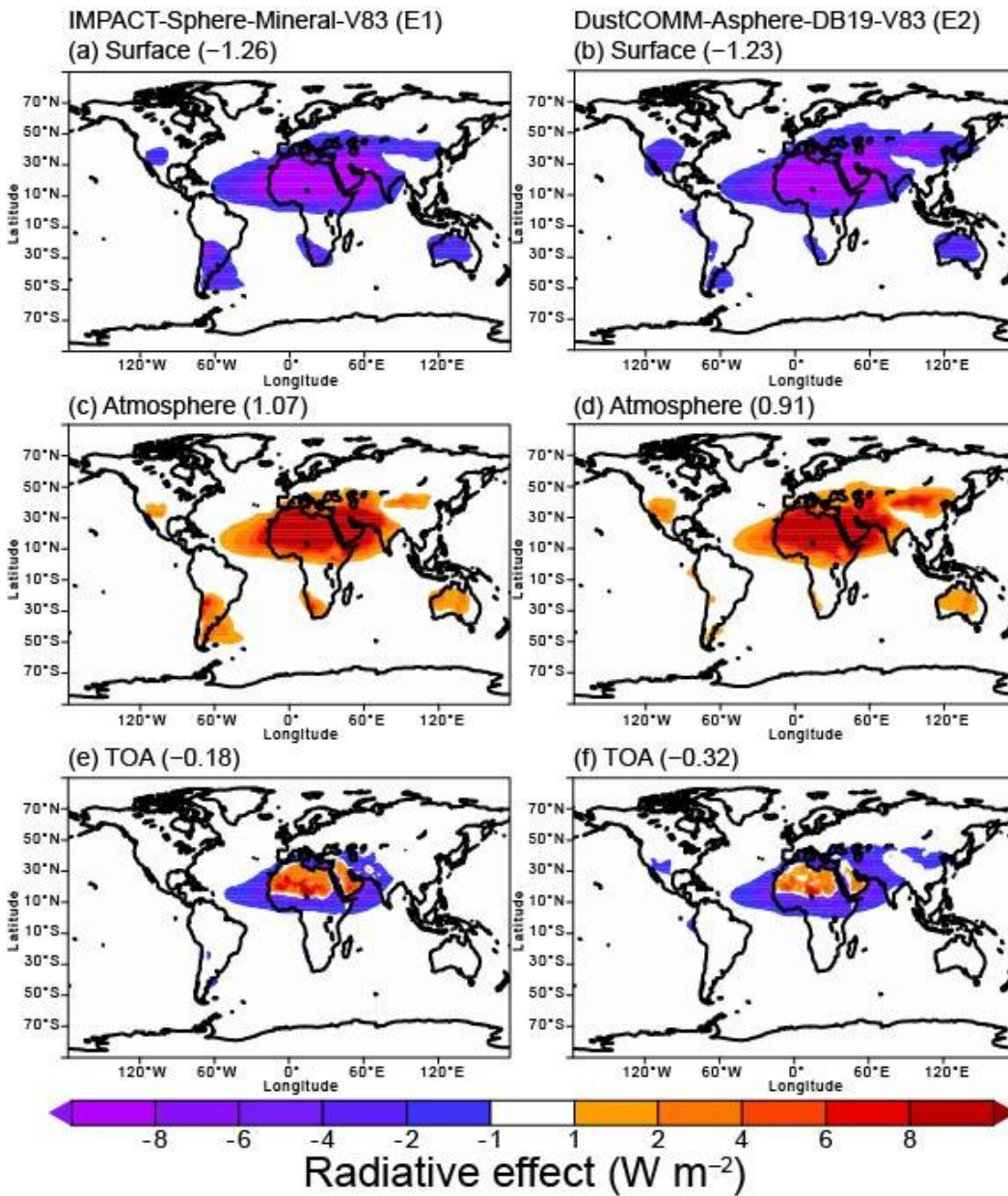


Figure 5. Summertime dDust clear-sky LW radiative effect efficiency ($W \cdot m^{-2} DAOD_{550}^{-1}$). Semi-observationally-based estimates at (a) surface and (b) TOA were based on satellite observations (Song et al., 2018; Christopher and Jones, 2007; Zhang and Christopher, 2003; Brindley and Russell, 2009; Yang et al., 2009). The model results were shown for (c) and (d) IMPACT-Sphere-Mineral-V83 (E1) default, and (e) and (f) DustCOMM-Asphere-DB19-V83 (E2) improved simulations at the surface and TOA, respectively. (g) Comparison of seasonally averaged LW radiative effect efficiency for semi-observationally-based (SOB) data and the different experiments. The square symbol represents the mean. The solid line within the box mark shows the median. The boundaries of the box mark the 25th and 75th percentiles. The whiskers above and below the box indicate the $1.5 \times$ interquartile range, and the points indicate the outside of the range. (h) Taylor diagram summarizing the statistics of the comparison against the seasonally averaged regional SW radiative effect efficiency for the different experiments. The horizontal axis shows the standard deviation of the data set or model prediction, the curved axis shows the correlation, and the green dashed lines denote the root-mean-squared errors between the semi-observationally-based data and the model predictions. As such, the distance between the semi-observationally-based data and the model predictions is a

70 ~~measure of the model's ability to reproduce the spatiotemporal variability in the semi-observationally-based data.~~ The regionally averaged values were listed in Tables S5 and S6 at the surface and TOA, respectively. ~~The scatter plot was shown in Fig. S4. The results from other sensitivity simulations were also shown in Fig. S5.~~



75 **Figure 6.** Dust SW radiative effect ($\text{W}\cdot\text{m}^{-2}$) and radiative heating of the atmosphere (i.e., the subtraction of radiative effects from TOA to the surface in unit of $\text{W}\cdot\text{m}^{-2}$). The model results were shown for the simulations for (a) [IMPACT-Sphere-Mineral-V83 \(E1\)_{default}](#) at the surface, (b) [DustCOMM-Asphere-DB19-V83 \(E2\)_{improved}](#) at the surface, (c) [E1_{default}](#) in atmospheric column, (d) [E2_{improved}](#) in atmospheric column, (e) [E1_{default}](#) at TOA, and (f) [E2_{improved}](#) simulations at TOA. The numbers in parentheses represented the global mean.

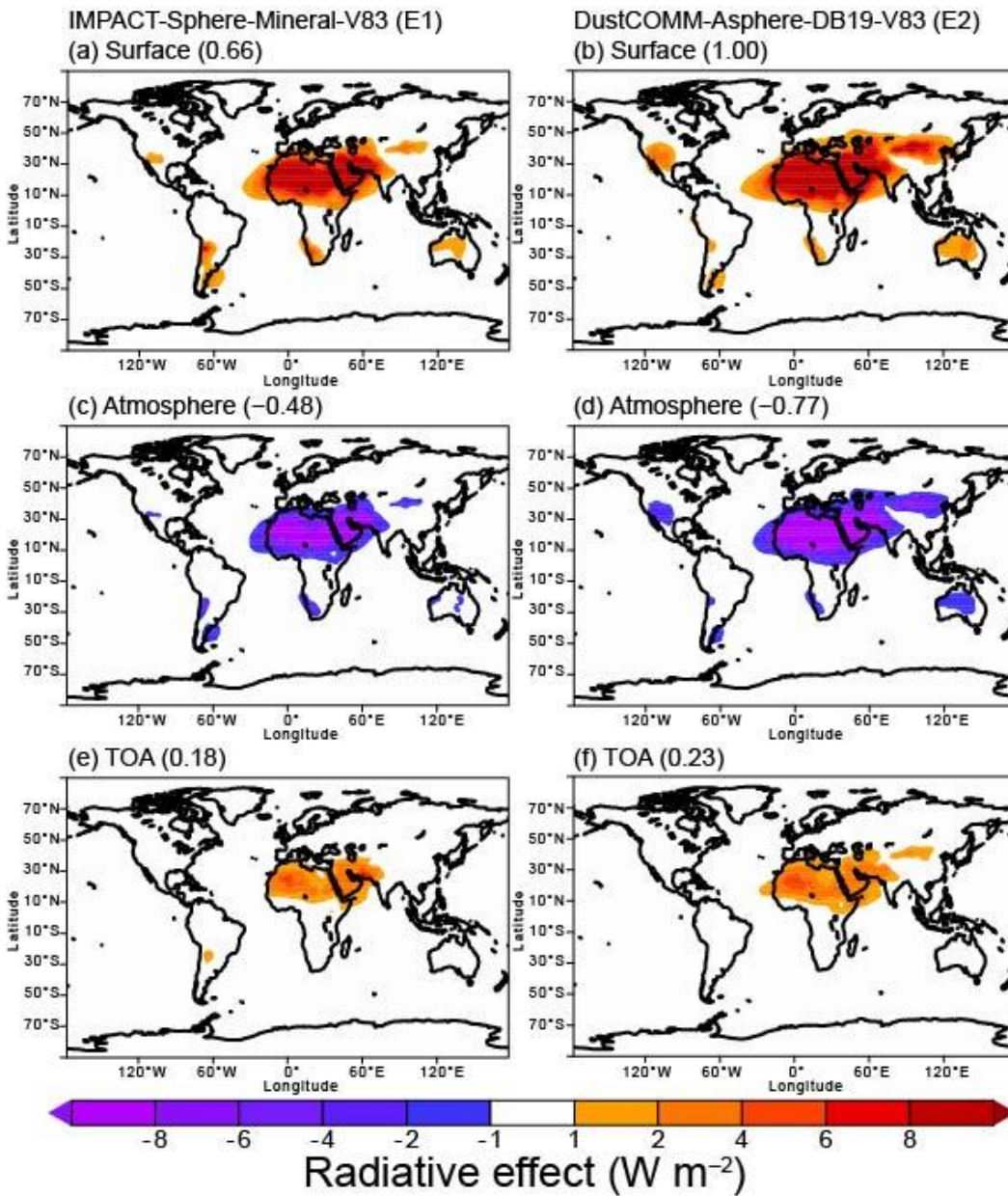
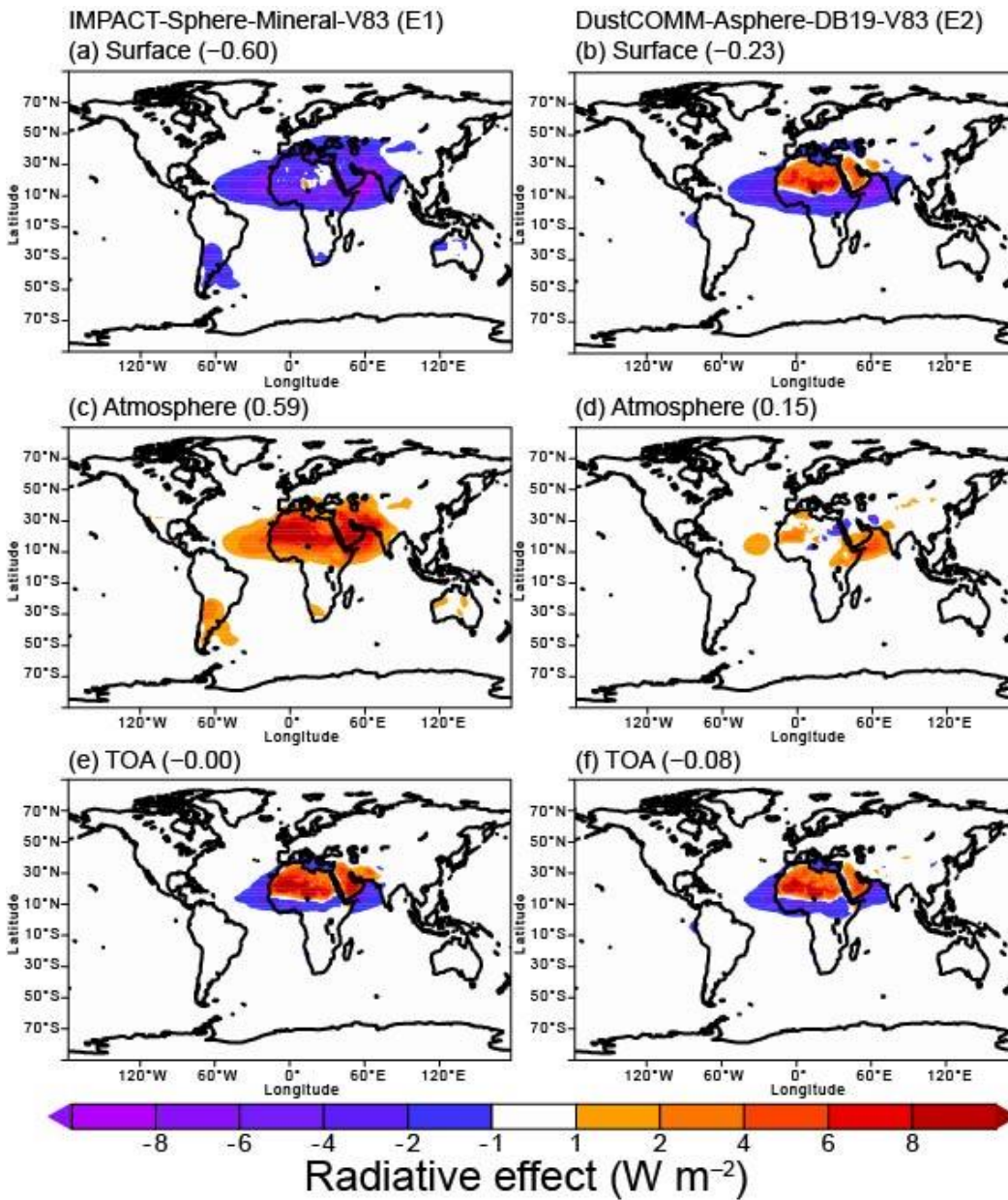
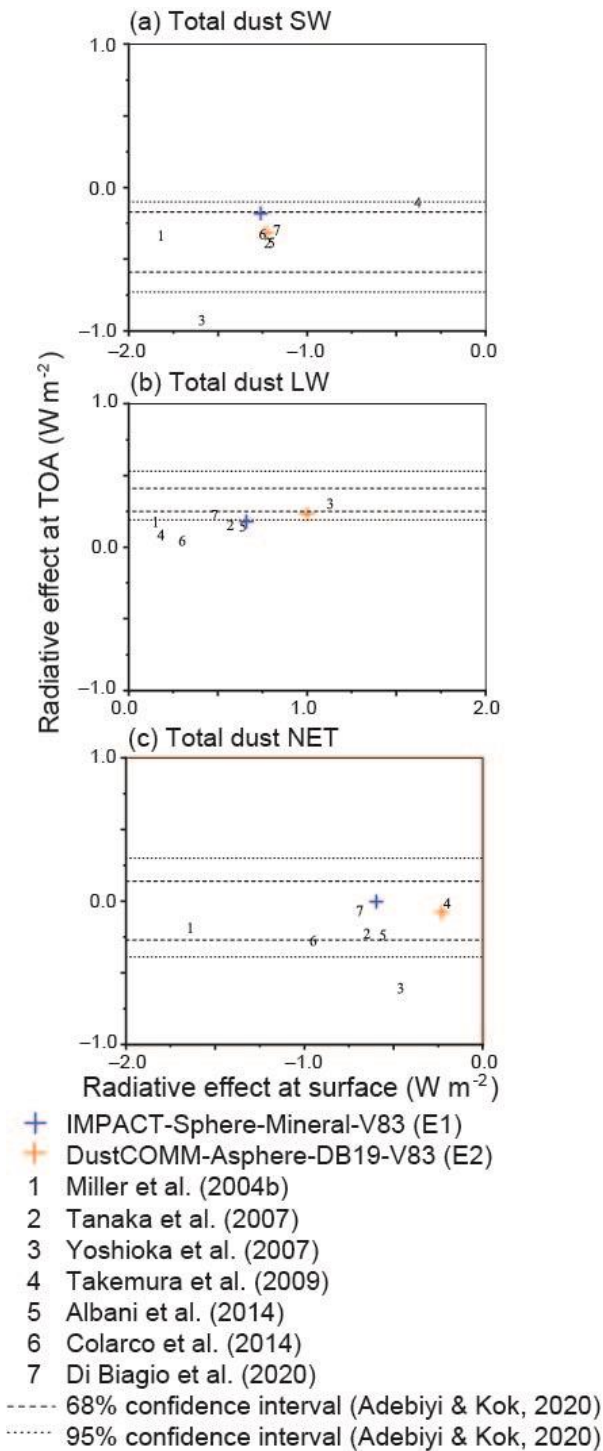


Figure 7. Dust LW radiative effect ($\text{W}\cdot\text{m}^{-2}$) and radiative heating of the atmosphere (i.e., the subtraction of radiative effects from TOA to the surface in unit of $\text{W}\cdot\text{m}^{-2}$). The model results were shown for the simulations for (a) [IMPACT-Sphere-Mineral-V83 \(E1\)_{default}](#) at the surface, (b) [DustCOMM-Asphere-DB19-V83 \(E2\)_{improved}](#) at the surface, (c) [E1_{default}](#) in atmospheric column, (d) [E2_{improved}](#) in atmospheric column, (e) [E1_{default}](#) at TOA, and (f) [E2_{improved}](#) simulations at TOA. The numbers in parentheses represented the global mean.



90 **Figure 8.** Dust radiative effect ($\text{W}\cdot\text{m}^{-2}$) and radiative heating of the atmosphere (i.e., the subtraction of radiative effects from TOA to the surface in unit of $\text{W}\cdot\text{m}^{-2}$). The model results were shown for the simulations for (a) [IMPACT-Sphere-Mineral-V83 \(E1\)_{default}](#) at the surface, (b) [DustCOMM-Asphere-DB19-V83 \(E2\)_{improved}](#) at the surface, (c) [E1_{default}](#) in atmospheric column, (d) [E2_{improved}](#) in atmospheric column, (e) [E1_{default}](#) at TOA, and (f) [E2_{improved}](#) simulations at TOA. The numbers in parentheses represented the global mean.



95 **Figure 9.** Radiative effect ($W\cdot m^{-2}$) of mineral dust due to different studies at the surface and TOA for (a) total dust SW, (b) total dust LW, and (c) total dust NET. The annually averaged values were listed in Table 5.

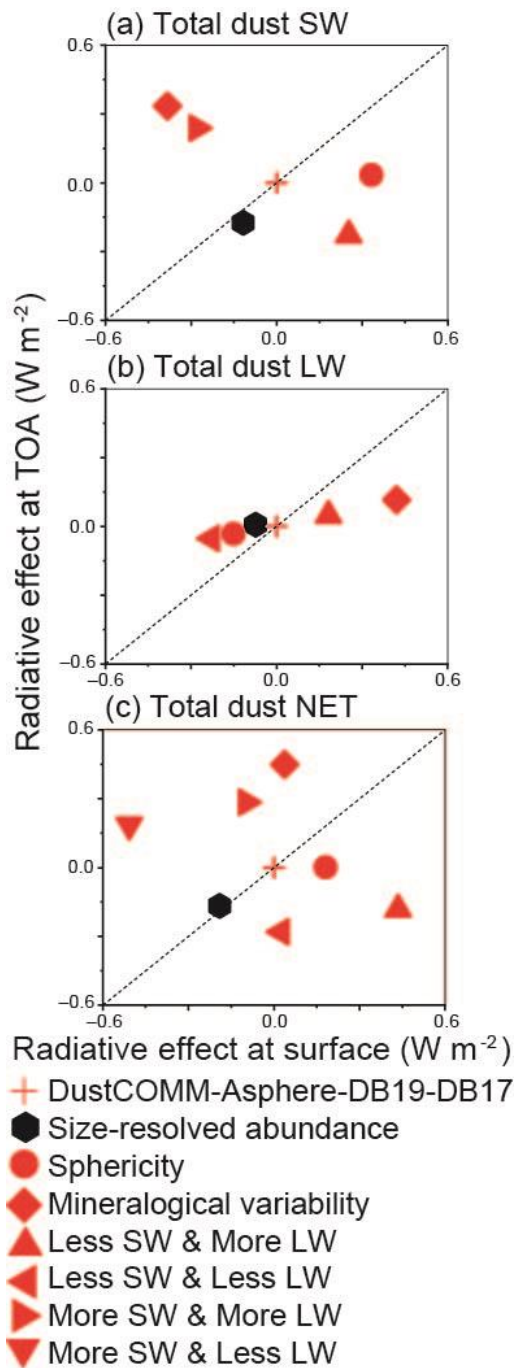


Figure 910. Radiative effect ($W \cdot m^{-2}$) of mineral dust due to various aerosol absorptivity at the surface and TOA for (a) total dust SW, (b) total dust LW, and (c) total dust NET. The annually averaged values were listed in Table 5. The dashed line represented a 1 : 1 correspondence and corresponded to no change in radiative heating within the atmosphere.